Explicit and Implicit Finite-Difference Methods for the Diffusion Equation in Two Dimensions

R. Schneider

Institut für Hochleistungsimpuls- und Mikrowellentechnik

Programm Kernfusion

Abstract

In this paper we focus our attention on rotationally symmetric problems, where cylinder coordinates are suitable. For Cartesian grid arrangements finite-difference schemes for the diffusion equation in two spatial dimensions are introduced. The temporal evolution is determined by implicit and explicit techniques. In addition to exactly solvable diffusion model problems we present numerical results of simulation experiments of a diamond disc window.

Explizite und implizite finite Differenzenmethoden zur Lösung der Diffusionsgleichung in zwei Raumdimensionen

Zusammenfassung

In diesem Bericht stehen rotationssymmetrische Diffusionsprobleme im Mittelpunkt, für welche Zylinderkoordinaten zur Beschreibung angemessen sind. Insbesondere werden für kartesische Gitteranordnungen Differenzenverfahren zur Lösung der Diffusionsgleichung in zwei Raumdimensionen vorgestellt. Zur zeitlichen Integration der semi-diskreten Gleichung werden sowohl implizite als auch explizite Techniken herangezogen. Exakt lösbare Diffusionsprobleme geben Auskunft über die Qualität, Eigenschaften und Verwendbarkeit der angewandten Lösungsmethoden. Ferner werden Resultate von Diamantfenster-Simulationen für verschiedene Parameterkonfigurationen präsentiert.

CONTENTS

1. INTRODUCTION

New ceramic materials are good candidates for vacuum windows of gyrotrons, barrier windows at the plasma torus and other applications in the enviroment of electron cyclotron resonance heating of plasmas in fusion energy research (see, e.g.[16, 19]). Detailed studies of the loss tangent, the thermal conductivity and further thermophysical properties of these windows are of great importance regarding their reliable usability. Transmission of MW power beams requires a suitable cooling system for each material. Hence, different window geometries have to be considered and compared. Numerical simulation is an appropriate and effective tool to investigate the thermal properties as well as to find the radial temperature distribution of disc windows having varying thickness and diameter. In order to perform the thermal analysis, a computer program has been developed. The description of the applied methods for the numerical solution of the time-dependent diffusion in two spatial dimensions is the main item of this report.

In the context of the present investigations, we focus our attention on rotationally symmetric problems, for which (z, r)-cylinder coordinates are a suitable choice. The computational domain is established by a Cartesian mesh, with a very clear and regular grid zone arrangement. Furthermore, finite-difference (FD) techniques are introduced to deal with the spatial derivatives of the diffusion equation. The temporal diffusion is modelled using an implicit as well as explicit approximation technique.

The organisation of this article is as follows: After the introduction of the governing equations of the two-dimensional rotationally symmetric diffusion problem in Section 2, the numerical framework for the diffusion equation is discussed in more detail in Section 3. There, the FD approach for the model equation is briefly outlined, the matrix-vector form of the semi-discrete diffusion equation is introduced and the implementation of some physically occuring as well as computational motivated boundary conditions are summarised. Furthermore, the temporal integration of the conservation equation is considered: This means that some basic explicit techniques are sketched and the implicit alternating-direction method is briefly reviewed. Some remarks on the stability of the considered schemes round off this section. Section 4 deals with numerical results obtained with the proposed methods. These simulation results demonstrate that the implemented algorithms produce accurate approximations and run in a very reliable manner. Subsequently in Section 5, numerical experiments for a synthetic diamond disc window are performed. For that purpose, the essential physical connections, which are necessary to simulate numerically the main features of heat transfer are briefly mentioned. Afterwards, numerical results of diamond window simulation experiments for different parameter configurations and boundary conditions are presented. Finally, concluding remarks and a short outlook for the further scientific goals are given in Section 6.

2. GOVERNING EQUATIONS

The heat transfer problem via conduction in the two-dimensional domain $\Omega \subset \mathbb{R}^2$ for cylinder coordinates $\mathbf{x} = (x_1, x_2)^T = (z, r)^T$ (see Figure 2.1) and $t > 0$ is mathematically modelled by the local diffusion equation (see, for instance [10])

$$\rho\, C_p\, \frac{\partial \theta(\mathbf{x}, t)}{\partial t} + \nabla \cdot \mathbf{h}(\mathbf{x}, t; \theta) = p_{eff}(\mathbf{x}, t; \theta)\ , \tag{2.1}$$

where $\theta(\mathbf{x}, t)$ ($[\theta] = K$) denotes the temperature field. The conduction is driven by an effective local power density $p_{eff}(\mathbf{x}, t; \theta)$ – also denoted as an effective source term — which depends on space, time and temperature and is measured in units of $[p_{eff}] = W/cm^3$. Furthermore, $\rho = \rho(\mathbf{x}; \theta)$ is the density ($[\rho] = g/cm^3$) and $C_p = C_p(\mathbf{x}; \theta)$ denotes the specific heat ($[C_p] = J/g/K$) of the considered materials. The heat flux vector function $\mathbf{h} = \mathbf{h}(\mathbf{x}, t; \theta)$ describes the heat flow through conduction ($[\mathbf{h}] = J/s/cm^2 = W/cm^2$) and is given by the linear Fourier law

$$\mathbf{h}(\mathbf{x}, t; \theta) = -\mathbb{S}(\mathbf{x}; \theta) \cdot \nabla \theta\ , \tag{2.2}$$

where the thermal conductivity tensor $\mathbb{S}$ depends, in general, on the temperature and, consequently, the conservation equation (2.1) establishes a nonlinear problem. For the following considerations we assume that the tensor $\mathbb{S}$ has a diagonal form

$$\mathbb{S}(\mathbf{x}; \theta) = \begin{pmatrix} \mathsf{s}_1(\mathbf{x}; \theta) & 0 \\ 0 & \mathsf{s}_2(\mathbf{x}; \theta) \end{pmatrix}\ , \tag{2.3}$$

where the thermal conductivities s_i are measured in $[\mathsf{s}_i] = W/cm/K$. From (2.2) and (2.3) we then obtain the equations

$$f(\mathbf{x}; \theta(\mathbf{x}, t)) \;=\; -\mathsf{s}_1(\mathbf{x}; \theta)\, \frac{\partial \theta(\mathbf{x}, t)}{\partial x_1}\ , \tag{2.4}$$

$$g(\mathbf{x}; \theta(\mathbf{x}, t)) \;=\; -\mathsf{s}_2(\mathbf{x}; \theta)\, \frac{\partial \theta(\mathbf{x}, t)}{\partial x_2}\ , \tag{2.5}$$

where the physical fluxes f and g are the components of the heat flux vector $\mathbf{h}$. Obviously, the energy conservation law established by the parabolic equation (2.1) has to be supplemented by appropriate initial data

$$\theta_0(\mathbf{x}) = \theta(\mathbf{x}, t = 0) \tag{2.6}$$

and by the boundary conditions, which are given for the cylinder symmetrical case by

$$\begin{aligned} g_1(x_2, t) &= \theta(z = 0, r, t)\ , \\ g_2(x_2, t) &= \theta(z = D, r, t)\ , \\ h_1(x_1, t) &= \theta(z, r = 0, t)\ , \\ h_2(x_1, t) &= \theta(z, r = R_0, t)\ . \end{aligned} \tag{2.7}$$

These boundary conditions for the computational domain Ω are schematically depicted in Figure 2.1. The special measurements of this domain of interest are discussed below for exactly solvable problems and are summarized in Table 5.1 for a praxis relevant problem. Furthermore, from our intention (cf., Figure 2.1) it is obvious, that the boundary function $h_1(x_1, t)$ coincides with the z-axis, which is the symmetry axis in our considerations.
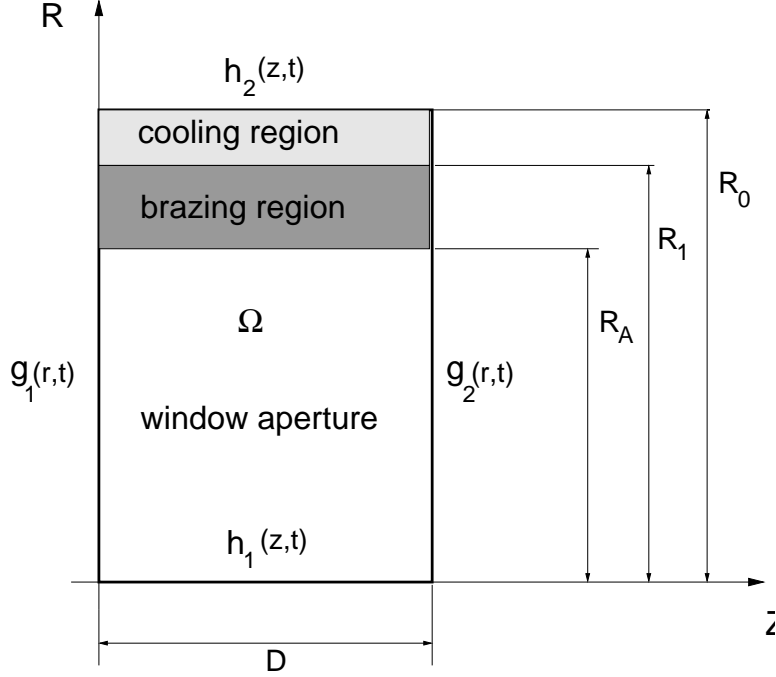
FIGURE 2.1. Computational domain Ω of a window disc with thickness D is schematically illustrated in the (z, r)-plain. The space and time dependent boundary data are denotd by g_i and h_i, respectively. For the geometrical parameters D, R_0, R_1 and R_A the values summarised in Table 5.1 are used.

2.1. **Assumptions and useful rearrangements.** Under the assumption that the system is rotationally symmetric with respect to the z-axis, then (z, r) - cylinder coordinates are obviously a suitable choice. In this case the divergence operator applied to the heat flux vector $\mathbf{h}$ is given

$$\nabla \cdot \mathbf{h} = \frac{\partial f}{\partial z} + \frac{1}{r} \frac{\partial}{\partial r} \left[r \, g \right] , \tag{2.8}$$

where the heat fluxes f and g are already specified by (2.4) and (2.5), respectively. We assume that the abbreviation

$$\xi(\theta) = \frac{1}{\rho \, C_p} \tag{2.9}$$

does not depend on the spatial coordinates, then the cylindrically symmetric conservation equation (2.1) can be recast into the following compact form

$$\frac{\partial \theta}{\partial t} = \frac{\partial F}{\partial z} + \frac{1}{r} \frac{\partial}{\partial r} \left[r \, G \right] + P_{eff} (\mathbf{x}, t; \theta) , \tag{2.10}$$

where the reduced physical heat fluxes are now determined by

$$F = S_1 (\mathbf{x}; \theta) \frac{\partial \theta}{\partial z} , \tag{2.11}$$

$$G = S_2 (\mathbf{x}; \theta) \frac{\partial \theta}{\partial r} , \tag{2.12}$$

3

and measured, respectively, in units of $[F] = [G] = cm \cdot K/s$. By doing this, the abbreviations

$$S_i(\mathbf{x}; \theta) = \xi(\theta)\, \mathsf{s}_i(\mathbf{x}; \theta)\ ; \quad i = 1, 2\ , \tag{2.13}$$

and

$$P_{eff}(\mathbf{x}, t; \theta) = \xi(\theta)\, p_{eff}(\mathbf{x}, t; \theta) \tag{2.14}$$

are introduced, which denote the reduced conductivities and effective power density. These new quantities (2.13) and (2.14) are measured in units of $[S_i] = \frac{cm^2}{s}$ and $[P_{eff}] = \frac{K}{s}$, respectively. Equation (2.10) holds for $0 < z < D$, $0 < r < R_0$ and $t > 0$. Since this equation is parabolic, the conditions (2.6) have to specified initially. Moreover, at the border of the computational domain appropriate boundary conditions (2.7) have to prescribed, which may depend, in general, on space and time. We emphasize that (2.10) is not true at the symmetry axis where $r = 0$. Assuming that $\partial\theta/\partial r = 0$ at $r = 0$ – which it will be if the problem is symmetrical with respect to the z-axis – then it is obvious that the flux G (2.12) vanishes if $r \to 0$. Performing a Taylor expansion of G around $r = 0$, we obtain

$$\lim_{r \to 0} \frac{G}{r} = \frac{\partial G}{\partial r}\big|_{r=0}\ , \tag{2.15}$$

and, consequently, the diffusion equation (2.10) now reads as

$$\frac{\partial\theta}{\partial t} = \frac{\partial F}{\partial z} + 2\,\frac{\partial G}{\partial r} + P_{eff}(\mathbf{x}, t; \theta)\ , \tag{2.16}$$

for $r \approx 0$ (on the symmetry axis). Clearly, the solution $\theta(\mathbf{x}, t)$ of the diffusion problem posed by (2.10) has to fulfil the latter equation (2.16) in the limit where r tends to zero.

We remark that in order to implement discrete circularly symmetric boundary conditions it is important to take the fact into account that the flux G is zero at the symmetry axis.

3. NUMERICAL FRAMEWORK FOR THE DIFFUSION EQUATION

In the following chapter we introduce a semi-discrete form of the conservation equation (2.1) in the domain Ω, which is conveniently written as

$$\frac{\partial\theta_{j,k}}{\partial t} = \mathcal{S}_{j,k}(t)\ , \tag{3.1}$$

for $j = 1, \ldots, J_m = J - 1$ and $k = 1, \ldots, K_m = K - 1$, where the right-hand side (rhs) $\mathcal{S}_{j,k}(t)$ is a suitable approximation of the physical fluxes and the effective local power density. For that, the approximation strategy applied to the conservation form is outlined for the cylinder symmetrical diffusion, where finite-diffference (FD) techniques are useful. In further subsections we present the temporal integration of the semi-discrete conservation law (3.1), where explicit as well as implicit numerical schemes are used.

3.1. **Spatial discretisation using the finite difference approach.**

3.1.1. *COMPUTATIONAL MESH.* In all cases the bounded domain of computation Ω is discretised in a simple manner by a Cartesian mesh as depicted in Figure 3.1. The nodes of the computational mesh are calculated according to
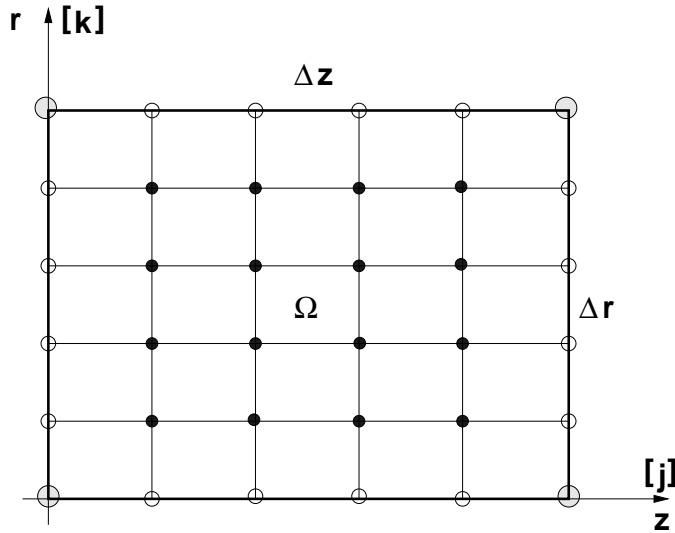

FIGURE 3.1. Schematic discretisation of the computational domain Ω.

$$z_j \quad = \quad z_0 + \Delta z \cdot j \ , \quad j = 0, 1, \dots J \ , \tag{3.2}$$

$$r_k \quad = \quad r_0 + \Delta r \cdot k \ , \quad k = 0, 1, \dots K \ , \tag{3.3}$$

where $(z_0 \, , r_0)$ are the coordinates of the starting point (left lower point) and Δz and Δr denote the equidistant spacing of the discretisation points along the z- and r-axis, respectively. The notation $r_{k+1/2}$, for instance, is an obvious abbreviation for the coordinate explicitly given by $r_{k+1/2} = r_0 + \Delta r \, (k + 1/2)$.

We remark, that in the context of the present paper only regular geometries are considered for which $(z, \ r)$ cylinder coordinates are the appropriate boundary-fitted numerical model of the computational domain. The treatment of irregular-shaped geometries within a simple Cartesian discretisation of the $(z, \ r)$-plain is postponed to a forthcoming article [13].

3.1.2. *NUMERICAL FLUX AND GRADIENT APPROXIMATION.* For the cylinder symmetrical problems in the $(z, \ r)$-plain, the rhs of the semi-discrete equation (3.1) is a direct approximation of the conservation equation (2.10) and reads as

$$\mathcal{S}_{j,k}(t) = \left. \frac{\partial F(t)}{\partial z} \right)_{j,k} + \left. \frac{1}{r} \frac{\partial}{\partial r} \left[r \, G(t) \right] \right)_{j,k} + \left. P_{eff} \left(\mathbf{x}, t; \theta \right) \right)_{j,k} , \tag{3.4}$$

where the fluxes are defined by (2.11) and (2.12), respectively. Clearly, we now have to specify how the approximations of the derivatives of the fluxes as well as of the fluxes itself should be performed. In both cases the standard central FD

approach is applied. Hence, the derivations with respect to the z-coordinate are approximated according to

$$\left.\frac{\partial F(t)}{\partial z}\right)_{j,k} = \frac{1}{\Delta z}\left[F_{j+1/2,k}(t) - F_{j-1/2,k}(t)\right] \tag{3.5}$$

with

$$F_{j+1/2,k}(t) = (S_1)_{j+1/2,k}\,\frac{1}{\Delta z}\left[\theta_{j+1,k}(t) - \theta_{j,k}(t)\right]\,, \tag{3.6}$$

while those with respect to the spatial r-coordinate are obtained by the following sequence of expressions

$$\left.\frac{1}{r}\frac{\partial}{\partial r}\left[r\,G(t)\right]\right)_{j,k} = \frac{1}{r_k}\frac{1}{\Delta r}\left[r_{k+1/2}\,G_{j,k+1/2}(t) - r_{k-1/2}\,G_{j,k-1/2}(t)\right] \tag{3.7}$$

with

$$G_{j,k+1/2}(t) = (S_2)_{j,k+1/2}\,\frac{1}{\Delta r}\left[\theta_{j,k+1}(t) - \theta_{j,k}(t)\right]\,. \tag{3.8}$$

We remark that the spatial dependence of the modified conductivities (2.13) is explicitly taken into account in the proposed approach. Furthermore, it is very convenient to use the abbreviation

$$\Sigma_{j,k} = \left(\beta_{j+1/2,k} + \beta_{j-1/2,k}\right) + \frac{1}{r_k}\left(\gamma_{j,k+1/2} + \gamma_{j,k-1/2}\right)\,, \tag{3.9}$$

where the coefficients β and γ are determined by

$$\beta_{j+1/2,k} = \frac{1}{(\Delta z)^2}(S_1)_{j+1/2,k} \tag{3.10}$$

and

$$\gamma_{j,k+1/2} = r_{k+1/2}\,\frac{1}{(\Delta r)^2}(S_2)_{j,k+1/2}\,, \tag{3.11}$$

respectively. The modified conductivities (2.13) are computed as average values at the intermediate location and are given by

$$(S_1)_{j+1/2,k} = \frac{1}{2}\left[(S_1)_{j+1,k} + (S_1)_{j,k}\right]\,, \tag{3.12}$$

$$(S_2)_{j,k+1/2} = \frac{1}{2}\left[(S_2)_{j,k+1} + (S_2)_{j,k}\right]\,. \tag{3.13}$$

Using these definitions and inserting them into the relations (3.5)-(3.8), we finally find for the rhs of the semi-discrete equation (3.1) in the cylinder symetrical case:

$$\begin{aligned}\mathcal{S}_{j,k}(t) =\ & \beta_{j-1/2,k}\,\theta_{j-1,k}(t) - \Sigma_{j,k}\,\theta_{j,k}(t) + \beta_{j+1/2,k}\,\theta_{j+1,k}(t)\\ & + \frac{\gamma_{j,k-1/2}}{r_k}\,\theta_{j,k-1}(t) + \frac{\gamma_{j,k+1/2}}{r_k}\,\theta_{j,k+1}(t) + \left[P_{eff}(t)\right]_{j,k}\,, \end{aligned} \tag{3.14}$$

where $\left[P_{eff}(t)\right]_{j,k}$ denotes the nodal approximation of the modified local power density (2.14). We note that the source (3.14) of the semi-discrete equation depends on the variables $\theta_{j,k}(t)$ lying inside the computational domain Ω. However, $\mathcal{S}_{j,k}(t)$ is also determined by the values $\theta_{0,k}(t)$, $\theta_{J,k}(t)$, $\theta_{j,0}(t)$ and $\theta_{j,K}(t)$, which are located at the border of the domain.

We finally remark that a Cartesian problem can be treated very similar to the cylinder symmetric case discussed in this section. This is managed by setting the

ratios $\frac{r_{k+1/2}}{r_k}$ and $\frac{r_{k-1/2}}{r_k}$ equal to one in the above given formulas. Therefore, the overall form of $\mathcal{S}_{j,k}(t)$ is the same for both Cartesian and cylinder coordinates.

3.1.3. *MATRIX-VECTOR FORM OF THE SEMI-DISCRETE DIFFUSION EQUATION.*

It is now desired to rewrite the semi-discrete equation (3.1) with the rhs (3.14) in order to obtain a compact matrix-vector formulation for this problem. To manage this task, we use a hierachical index organisation of the form

$$\forall i: \quad i = J_m \, (k-1) + j \quad \text{with } j = 1, \ldots, J_m; \quad k = 1, \ldots, K_m \tag{3.15}$$

to express $\mathcal{S}_{j,k}(t)$ in terms of a matrix and vectors. Moreover, it is useful to separate the nodes inside the domain Ω from these one located at the border $\partial\Omega$ of the computational domain (cf., Figure 3.1). For the nodes located in the interior of Ω, it is easy to verify that the rhs (3.14) $-$ without $\left[P_{eff}(t)\right]_{j,k}$ $-$ can be brought into the form

$$\mathbb{A} \cdot \mathbf{w}(t) \,, \tag{3.16}$$

where $\mathbb{A}$ is a sparse, penta-diagonal matrix and $\mathbf{w}(t)$ denotes the solution vector. This variable vector has the structure

$$\mathbf{w}(t) = \left(\theta_{1,1}, \, \ldots, \, \theta_{J_m,1}, \, \theta_{1,2}, \, \ldots, \, \theta_{J_m,2}, \, \ldots, \, \theta_{1,K_m}, \, \ldots, \, \theta_{J_m,K_m}\right)^T \,, \tag{3.17}$$

from which it is clear that the length of the column vector $\mathbf{w}$ is $J_m \cdot K_m$, so that $\mathbf{w} \in \mathbb{R}^{J_m \cdot K_m}$. The explicit block structure of the sparse matrix $\mathbb{A}$, consisting of $K_m = K - 1$ main diagonal blocks, is given by

$$\mathbb{A} = \begin{pmatrix} \mathbb{D}_1 & \mathbb{U}_1 & 0 & 0 & 0 & \ldots & 0 \\ \mathbb{L}_2 & \mathbb{D}_2 & \mathbb{U}_2 & 0 & 0 & \ldots & 0 \\ 0 & \mathbb{L}_3 & \mathbb{D}_3 & \mathbb{U}_3 & 0 & \ldots & 0 \\ \vdots & & \ddots & \ddots & \ddots & & \vdots \\ 0 & 0 & 0 & 0 & \mathbb{L}_{K_m-1} & \mathbb{D}_{K_m-1} & \mathbb{U}_{K_m-1} \\ 0 & 0 & 0 & 0 & 0 & \mathbb{L}_{K_m} & \mathbb{D}_{K_m} \end{pmatrix} \,, \tag{3.18}$$

where the diagonal block matrices $\mathbb{D}_k \in \mathbb{R}^{J_m \times J_m}$, $k = 1, \ldots, K_m$, with a block size of $J_m \times J_m = (J-1) \times (J-1)$ possesses a tridiagonal character

$$\mathbb{D}_k = \begin{pmatrix} -\Sigma_{1,k} & \beta_{3/2,k} & 0 & 0 & 0 & \ldots & 0 \\ \beta_{3/2,k} & -\Sigma_{2,k} & \beta_{5/2,k} & 0 & 0 & \ldots & 0 \\ 0 & \beta_{5/2,k} & -\Sigma_{3,k} & \beta_{7/2,k} & 0 & \ldots & 0 \\ \vdots & & \ddots & \ddots & \ddots & & \vdots \\ 0 & 0 & 0 & 0 & \beta_{J_m-3/2,k} & -\Sigma_{J_m-1,k} & \beta_{J_m-1/2,k} \\ 0 & 0 & 0 & 0 & 0 & \beta_{J_m-1/2,k} & -\Sigma_{J_m,k} \end{pmatrix} \,. \tag{3.19}$$

The lower and upper block matrices $\mathbb{L}_k$ and $\mathbb{U}_k$ with $\mathbb{L}_k$, $\mathbb{U}_k \in \mathbb{R}^{J_m \times J_m}$ are simple diagonal matrices of the form

$$\mathbb{L}_{k+1} = \mathbb{U}_k = \text{diag}\left(\gamma_{1,k+1/2}, \, \gamma_{2,k+1/2}, \, \ldots, \, \gamma_{J_m,k+1/2}\right); \quad k = 1, \ldots, \, K_m \,. \tag{3.20}$$

The entries of the matrices $\mathbb{D}_k$, $\mathbb{L}_k$ and $\mathbb{U}_k$ are computed with the aid of the relations (3.9)-(3.11). In addition to the inner nodes of Ω, we have to consider those lying at the border $\partial\Omega$, since the source $\mathcal{S}_{j,k}(t)$ also depends on these boundary values.

After some rearrangements of the equation (3.14), we observe that it is possible to combine the boundary value dependent terms in a vector of the form

$$
\mathbf{B}(t) = \begin{pmatrix} \mathbf{b}_1 \\ \mathbf{b}_2 \\ \vdots \\ \mathbf{b}_{K_m-1} \\ \mathbf{b}_{K_m} \end{pmatrix}^T , \qquad (3.21)
$$

where the column vectors $\mathbf{b}_k \in \mathbb{R}^{J_m}$ are computed by the prescrition

$$
\mathbf{b}_1 = \begin{pmatrix} \beta_{1/2,1}\,\theta_{0,1} + \frac{\gamma_{1,1/2}}{r_1}\,\theta_{1,0} \\ \frac{\gamma_{2,1/2}}{r_1}\,\theta_{2,0} \\ \vdots \\ \frac{\gamma_{J_m-1,1/2}}{r_1}\,\theta_{J_m-1,0} \\ \beta_{J_m+1/2,1}\,\theta_{J_m+1,1} + \frac{\gamma_{J_m,1/2}}{r_1}\,\theta_{J_m,0} \end{pmatrix} , \qquad (3.22)
$$

$$
\mathbf{b}_{K_m} = \begin{pmatrix} \beta_{1/2,K_m}\,\theta_{0,K_m} + \frac{\gamma_{1,K_m+1/2}}{r_{K_m}}\,\theta_{1,K_m+1} \\ \frac{\gamma_{2,K_m+1/2}}{r_{K_m}}\,\theta_{2,K_m+1} \\ \vdots \\ \frac{\gamma_{J_m-1,K_m+1/2}}{r_{K_m}}\,\theta_{J_m-1,K_m+1} \\ \beta_{J_m+1/2,K_m}\,\theta_{J_m+1,K_m} + \frac{\gamma_{J_m,K_m+1/2}}{r_{K_m}}\,\theta_{J_m,K_m+1} \end{pmatrix} , \qquad (3.23)
$$

and

$$
\mathbf{b}_k = \begin{pmatrix} \beta_{1/2,k}\,\theta_{0,k} \\ 0 \\ \vdots \\ 0 \\ \beta_{J_m+1/2,k}\,\theta_{J_m+1,k} \end{pmatrix} , \quad k = 2,3,\ldots,K_m - 1 . \qquad (3.24)
$$

In the following the vector $\mathbf{B}(t)$ is called the boundary vector which, in general, depends on time. For sake of completness, the effective local power density vector is introduced by

$$
\mathbf{P}_{eff}(t) = \Big([P_{eff}]_{1,1}, \ldots, [P_{eff}]_{J_m,1}, \ldots, [P_{eff}]_{1,K_m}, \ldots, [P_{eff}]_{J_m,K_m}\Big)^T , \qquad (3.25)
$$

and depends also on time and, in general, on the temperature field $\theta_{j,k}(t)$. Combining the results discussed above, we obtain the following matrix-vector formulation for the semi-discrete form of the diffusion equation (2.1)

$$
\frac{d}{dt}\mathbf{w}(t) = \mathbf{S}(t;\mathbf{w}) \qquad (3.26)
$$

$$
\mathbf{S}(t;\mathbf{w}) = \mathbb{A} \cdot \mathbf{w}(t) + \mathbf{B}(t) + \mathbf{P}_{eff}(t) , \qquad (3.27)
$$

where the time-dependent variable vector $\mathbf{w}(t) \in \mathbb{R}^{J_m \cdot K_m}$ is defined by equation (3.17). It is obvious from this formulation that the source vector $\mathbf{S}(t;\mathbf{w}) \in \mathbb{R}^{J_m \cdot K_m}$ depends explicitly on the solution vector $\mathbf{w}(t)$ as well as on the time-dependent boundary $\mathbf{B}(t) \in \mathbb{R}^{J_m \cdot K_m}$ and on the power density $\mathbf{P}_{eff}(t) \in \mathbb{R}^{J_m \cdot K_m}$ vector. Furthermore, we note that (3.26) represents nothing else than a system of ordinary differential equations, which can be numerically treated with standard techniques

if appropriate initial data are prescribed. Some of these – more or less – standard methods are briefly sketched below in Section 4.2.

3.1.4. *BOUNDARY CONDITIONS AND THEIR IMPLEMENTATION.* In the following discussion, we describe the numerical implementation of physically occuring as well as computationally motivated boundary conditions in the FD context. For that purpose, we divide the boundary surface $\partial\Omega$ of the computational domain Ω into, for instance, three disjoint subsets Γ_T, Γ_R and Γ_S representing a thermally insulated, a radiating and a circular symmetric surface, respectively, where $\partial\Omega = \Gamma_T \cup \Gamma_R \cup \Gamma_S$.

- **Thermally insulated surface:**
  This condition occurs very frequently in practice and is expressed in terms of derivatives. A heat-conducting material is said to be thermally insulated, if there is no heat flow normal to a surface. This situation should be established by the fact that at the corresponding boundary the condition

  $$\frac{\partial\theta}{\partial n}\Big|_{\Gamma_T} = \mathbf{n} \cdot \nabla\theta\big|_{\Gamma_T} = 0 \qquad (3.28)$$

  is enforced at every point of the insulated surface Γ_T, where $\mathbf{n}$ denotes the outwards directed unit normal at this surface. For cylinder coordinates with $\mathbf{n} = -\mathbf{e}_z = (-1,\,0)^T$, for instance, we obtain from (3.28) the condition

  $$\frac{\partial\theta(r,t)}{\partial z}\Big|_{z=0} = 0 \qquad (3.29)$$

  for the temperature, which may depend on r as well as t. Obviously, the latter condition can be used to specify the border function $g_1(r,t)$ given by (2.7) for the thermally insulated situation. Applying a central difference formula, the condition (3.29) is numerically modelled by

  $$\frac{1}{2\,\Delta z}\left(\theta_{1,k}^n - \theta_{-1,k}^n\right) = 0 \iff \theta_{-1,k}^n = \theta_{1,k}^n \quad \forall k \,. \qquad (3.30)$$

  Then, the boundary values are computed from the averaging

  $$\theta_{0,k}^n = \frac{1}{2}\left(\theta_{1,k}^n + \theta_{-1,k}^n\right)\,, \qquad (3.31)$$

  yielding finally the desired boundary data

  $$\theta_{0,k}^n = \theta_{1,k}^n \iff g_1(r_k, t^n) = \theta_{1,k}^n \quad \forall k \qquad (3.32)$$

  at the time level $t = t^n$. We note that the boundary condition (3.28) simply represents a Neumann condition for the temperature at the border Γ_T of the domain.

- **Surface cooling:**
  The rate of (heat) energy flow across any surface in the direction of the outwards normal $\mathbf{n}$ is given by

  $$\mathbf{n} \cdot \mathbf{h}\big|_{\Gamma_R} = -\mathbf{n} \cdot \left[\mathbb{S} \cdot \nabla\theta\right]\big|_{\Gamma_R}\,, \qquad (3.33)$$

  where the fundamental Fourier law (2.2) is used. It is often assumed that this energy transfer from the boundary surface Γ_R at temperature θ into the surrounding medium at temperature θ_{cool} is modelled according to

  $$-\mathbf{n} \cdot \left[\mathbb{S} \cdot \nabla\theta\right]\big|_{\Gamma_R} = \alpha\left(\theta - \theta_{cool}\right)\,, \qquad (3.34)$$

where α ($[\alpha] = W/cm^2/K$) denotes the coefficient of heat transfer for the materials of interset. Obviously, this ansatz may also be interpreted as an inhomogeneous Neumann boundary condition. For the moment we consider the cylinder symmetrical case, where the normal is determined by $\mathbf{n} = \mathbf{e}_r = (0, 1)^T$ and the boundary Γ_R is explicitly specified by $r = R_0$ (cf. Figure 2.1). Consequently, we obtain from (3.34) the relation

$$-\mathsf{s}_2 \frac{\partial \theta(z, t)}{\partial r}\Big|_{r=R_0} = \alpha \left(\theta - \theta_{cool} \right) , \qquad (3.35)$$

which is the starting point to define the function $h_2(z, t)$ (cf., (2.7)), where s_2 denotes the conductivity (cf., (2.3)). We assume that the semi-discrete equation (3.1) does not hold at $r = R_0$. Hence, equation (3.35) is the needed additional relation in order to fix the boundary temperature. A suitable numerical estimation of this temperature may be obtained by using (the less accurate) forward differencing approach. Consequently, we find for the updating of the boundary data at $r = R_0$ the expression

$$h_2(z_j, t^n) = \theta_{j,K-1}^n - \Delta r \frac{\alpha}{(\mathsf{s}_2)_{j,K-1}} \left[\theta_{j,K-1}^n - (\theta_{cool})_{j,K}^n \right] \qquad (3.36)$$

at the time level $t = t^n$ for all j. Numerical experiments indicate that for most practical applications the accuraccy of the latter approximation is sufficient.

- **Circular symmetry condition:**
  As already mentioned above in Section 2.1, the basic diffusion equation (2.10) has to be replaced by the conservation equation (2.16) at the symmetry axis. To model numerically the symmetry condition at $r = 0$ (the origin of the (r, φ)-plane), we assume that the flux G vanishes at Γ_S if r tend to zero, which means that

$$G_{j,0}(t) = \frac{1}{2} \left[G_{j,1/2}(t) + G_{j,-1/2}(t) \right] \equiv 0 \qquad (3.37)$$

at the time t. Using the definition (3.8) and performing some rearrangements, we obtain the relation

$$\left[(S_2)_{j,-1/2} - (S_2)_{j,1/2} \right] \theta_{j,0}(t) = (S_2)_{j,-1/2}\, \theta_{j,-1}(t) - (S_2)_{j,1/2}\, \theta_{j,1}(t) \qquad (3.38)$$

for the symmetry axis temperature $\theta_{j,0}(t)$, which depends especially on $\theta_{j,-1}(t)$. For problems symmetrical with respect to the z-axis $\frac{\partial \theta}{\partial r} = 0$ at $r = 0$. Consequently, from the discrete version of this relation we find that

$$\theta_{j,-1}(t) = \theta_{j,1}(t) \qquad (3.39)$$

holds. Inserting this result into the relation (3.38) we immediately obtain the temporal updating prescription

$$h_1(z_j, t) = \theta_{j,1}(t) ; \quad \forall t \geq 0 , \qquad (3.40)$$

which is valid for all $j = 1, \ldots, J_m$ at the symmetry axis Γ_S located at $r = 0$. As a consequence that the derivative with respect to r vanishes, the boundary condition at the symmetry axis (3.40) represents once again a Neumann condition for $\theta(\mathbf{x}, t)$ at the border Γ_S of the computational domain.

3.2. Temporal integration of the conservation law.

3.2.1. *EXPLICIT TECHNIQUES.* The matrix-vector formulation of the semi-discrete diffusion equation given by (3.26) and (3.27) establishes an initial value problem for a system of ordinary differential equations. To attack such a system of differential equations numerically, a lot of standard solvers are available (see, e.g. [11, 17, 8, 5]). In this section we sketch out very briefly some basic integration techniques, which are frequently used in the context of the present investigations to solve the semi-discrete diffusion equation numerically. For the subsequent discussions we start from equation (3.26) with the source (3.27) and assume that the initial data – abbreviated by $\mathbf{w}^0 = \mathbf{w}(t_0)$ – are given.

- Modified Euler Scheme:
  In this approach an estimated value is computed for the next time level. Afterwards an averaging yields the solution at the new time level t^{n+1}. The algorithm reads as (see, for instance, [5])

$$\tilde{\mathbf{w}}^{n+1} = \mathbf{w}^n + \Delta t\,\mathbf{S}(t^n; \mathbf{w}^n) \qquad (3.41)$$

$$\mathbf{w}^{n+1} = \mathbf{w}^n + \frac{\Delta t}{2}\Big[\mathbf{S}(t^n; \mathbf{w}^n) + \mathbf{S}(t^{n+1}; \tilde{\mathbf{w}}^{n+1})\Big] , \qquad (3.42)$$

  and preserves globally second-order accuracy with respect to time. The local approximation error is of the order $\mathcal{O}(\Delta t^3)$.

- Heun Scheme:
  The Heun approach [5] may be written in the following way

$$\tilde{\mathbf{w}}^{n+2/3} = \mathbf{w}^n + \frac{2}{3}\Delta t\,\mathbf{S}(t^n; \mathbf{w}^n) \qquad (3.43)$$

$$\mathbf{w}^{n+1} = \mathbf{w}^n + \frac{\Delta t}{4}\Big[\mathbf{S}(t^n; \mathbf{w}^n) + 3\,\mathbf{S}(t^{n+2/3}; \tilde{\mathbf{w}}^{n+2/3})\Big] , \qquad (3.44)$$

  where $t^{n+2/3}$ is the abbreviation for $t^{n+2/3} = t^n + 2/3\,\Delta t$. This scheme is also globally second-order accurate and the local approximation is $\mathcal{O}(\Delta t^3)$.

- TVD Runge-Kutta Technique:
  Very resently Shu and Osher introduced a new class of modified Runge-Kutta methods which preserves the so-called TVD property [14, 15, 7]. From the family of these special methods, this two-stage scheme with an approximation order of two reads as

$$\tilde{\mathbf{w}}^{n+1} = \mathbf{w}^n - \Delta t\,\mathbf{S}(t^n; \mathbf{w}^n) \qquad (3.45)$$

$$\mathbf{w}^{n+1} = \frac{1}{2}\mathbf{w}^n + \frac{1}{2}\tilde{\mathbf{w}}^{n+1} - \frac{1}{2}\Delta t\,\mathbf{S}(t^{n+1}; \tilde{\mathbf{w}}^{n+1}) . \qquad (3.46)$$

- Classical Runge-Kutta Approach:
  This well-know classical four-step method [11, 5] is globally fourth-order

accurate and may be written as

$$\begin{aligned}
\mathbf{K}_1 &= \mathbf{S}(t^n; \mathbf{w}^n) \\
\mathbf{K}_2 &= \mathbf{S}(t^{n+1/2}; \mathbf{w}^n + \frac{\Delta t}{2}\mathbf{K}_1) \\
\mathbf{K}_3 &= \mathbf{S}(t^{n+1/2}; \mathbf{w}^n + \frac{\Delta t}{2}\mathbf{K}_2) \\
\mathbf{K}_4 &= \mathbf{S}(t^{n+1}; \mathbf{w}^n + \Delta t\mathbf{K}_3) \qquad\qquad (3.47) \\
\mathbf{w}^{n+1} &= \mathbf{w}^n + \frac{\Delta t}{6}\Big[\mathbf{K}_1 + 2\,\mathbf{K}_2 + 2\,\mathbf{K}_3 + \mathbf{K}_4\Big] , \qquad (3.48)
\end{aligned}$$

with $t^n = t_0 + \Delta t\, n$. Furthermore, the order of the local approximation is $\mathcal{O}(\Delta t^5)$.

3.2.2. *IMPLICIT APPROACH.* Somtimes a disadvantage of explicit methods is the time step size requirement due to the Courant-Friedrichs-Lewy (CFL) condition [3]. In order to circumvent this stability restriction it is common to rely on implicit schemes which, in addition, possesses the property of high stability. Usually diffusion problems are best treated by applying implicit methods, which are second-order accurate in both space and time. A recommended approach [11] to solve numerically the diffusion equation is the implicit Crank-Nicholson scheme [4, 1, 11, 17]. A consequence of the implicit differencing is that a system of coupled linear equations has to be solved. In one space dimension the resulting system has a tridiagonal form. However, this is no longer true in multidimensions, where the matrix is still sparse but not tridiagonal. In this report we use a slightly modified Crank-Nicholson scheme in two dimensions: Each time step Δt is divided into two substeps of size $\Delta t/2$, where, respectively, a different spatial dimension is approximated in an implicit way. Conceptually this approach is an operator splitting technique, which may be called as alternating-direction implicit method (ADI). A decisive advantage of the ADI concept is that only a tridiagonal system has to be solved in each substep. An implicit scheme, second-order in time and space is, for instance, proposed in [11]. This very accurate and stable algorithm is adopted for our purposes and reads in rewritten form as

Step I:

$$\begin{aligned}
\frac{2}{\Delta t}\left(\theta_{j,k}^{n+1/2} - \theta_{j,k}^n\right) &= \frac{1}{\Delta z}\left(F_{j+1/2,k}^{n+1/2} - F_{j-1/2,k}^{n+1/2}\right) \\
&+ \frac{1}{\Delta r}\left(\frac{r_{k+1/2}}{r_k}G_{j,k+1/2}^n - \frac{r_{k-1/2}}{r_k}G_{j,k-1/2}^n\right) \\
&+ \left[P_{eff}\right]_{j,k}^n , \qquad\qquad\qquad (3.49)
\end{aligned}$$

Step II:

$$\begin{aligned}
\frac{2}{\Delta t}\left(\theta_{j,k}^{n+1} - \theta_{j,k}^{n+1/2}\right) &= \frac{1}{\Delta z}\left(F_{j+1/2,k}^{n+1/2} - F_{j-1/2,k}^{n+1/2}\right) \\
&+ \frac{1}{\Delta r}\left(\frac{r_{k+1/2}}{r_k}G_{j,k+1/2}^{n+1} - \frac{r_{k-1/2}}{r_k}G_{j,k-1/2}^{n+1}\right) \\
&+ \left[P_{eff}\right]_{j,k}^{n+1/2} . \qquad\qquad\qquad (3.50)
\end{aligned}$$

Here, the rhs (3.4) of the semi-discrete equation (3.1) is approximated in two steps, where the discretisation of fluxes F and G are given by (3.6) and (3.8), respectively. For further reformulations of the latter two equations, it is convenient to introduce the following notations

$$b_{j+1/2,k} = \frac{\Delta t}{2\,(\Delta z)^2} \Big(S_1\Big)_{j+1/2,k} , \qquad (3.51)$$

$$c_{j,k+1/2} = r_{k+1/2}\,\frac{\Delta t}{2\,(\Delta r)^2} \Big(S_2\Big)_{j,k+1/2} , \qquad (3.52)$$

$$B_{j,k} = b_{j+1/2,k} + b_{j-1/2,k} , \qquad (3.53)$$

$$C_{j,k} = \frac{1}{r_k} \Big(c_{j,k+1/2} + c_{j,k-1/2}\Big) , \qquad (3.54)$$

where $\Big(S_1\Big)_{j+1/2,k}$ and $\Big(S_2\Big)_{j,k+1/2}$ are given by (3.12) and (3.13), respectively. Using these abbreviations and performing some rearrangements, we obtain from (3.49) and (3.50) the two recurrence relations

$$-b_{j-1/2,k}\,\theta_{j-1,k}^{n+1/2} + \Big(1 + B_{j,k}\Big)\theta_{j,k}^{n+1/2} \quad - \quad b_{j+1/2,k}\,\theta_{j+1,k}^{n+1/2} =$$
$$\frac{c_{j,k-1/2}}{r_k}\,\theta_{j,k-1}^{n} + \Big(1 - C_{j,k}\Big)\theta_{j,k}^{n} \quad + \quad \frac{c_{j,k+1/2}}{r_k}\,\theta_{j,k+1}^{n}$$
$$+ \quad \frac{\Delta t}{2}\,\big[P_{eff}\big]_{j,k}^{n} , \qquad (3.55)$$

and

$$-\frac{c_{j,k-1/2}}{r_k}\,\theta_{j,k-1}^{n+1} + \Big(1 + C_{j,k}\Big)\theta_{j,k}^{n+1} \quad - \quad \frac{c_{j,k+1/2}}{r_k}\,\theta_{j,k+1}^{n+1} =$$
$$b_{j-1/2,k}\,\theta_{j-1,k}^{n+1/2} + \Big(1 - B_{j,k}\Big)\theta_{j,k}^{n+1/2} \quad + \quad b_{j+1/2,k}\,\theta_{j+1,k}^{n+1/2}$$
$$+ \quad \frac{\Delta t}{2}\,\big[P_{eff}\big]_{j,k}^{n+1/2} \qquad (3.56)$$

for the unknowns $\theta_{j,k}^{n+1}$. In the following we rewrite both relations in order to get a very compact matrix-vector formulation of this ADI method. For that, the vector of the variables $\theta_{j,k}^{n+1/2}$ at the intermediate time level $t = t^{n+1/2}$ may be written as

$$\mathbf{w}^{n+1/2} = \Big(\theta_{1,1}^{n+1/2},\,\ldots,\,\theta_{J_m,1}^{n+1/2};\,\ldots;\,\theta_{1,K_m}^{n+1/2},\,\ldots,\,\theta_{J_m,K_m}^{n+1/2}\Big)^{T} \in \mathbb{R}^{J_m\cdot K_m} , \quad (3.57)$$

where the indices j and k obviously run according to $j = 1,\,\ldots,\,J_m = J - 1$ and $k = 1,\,\ldots,\,K_m = K - 1$. With this in mind, we can define a sparse tridiagonal matrix

$$\mathbb{T} = \begin{pmatrix} \mathbb{M}_1 & 0 & 0 & 0 & 0 & \ldots & 0 \\ 0 & \mathbb{M}_2 & 0 & 0 & 0 & \ldots & 0 \\ 0 & 0 & \mathbb{M}_3 & 0 & 0 & \ldots & 0 \\ \vdots & & \ddots & \ddots & \ddots & & \vdots \\ 0 & 0 & 0 & 0 & 0 & \mathbb{M}_{K_m-1} & 0 \\ 0 & 0 & 0 & 0 & 0 & 0 & \mathbb{M}_{K_m} \end{pmatrix} , \qquad (3.58)$$

which possesses $K_m = K - 1$ block matrices along the diagonal. The explicit structure of such a diagonal block matrix $\mathbb{M}_k \in \mathbb{R}^{J_m \times J_m}$, $k = 1,\,\ldots,\,K_m$ is found

to be

$$
\mathbb{M}_k \;=\; \begin{pmatrix}
1 + B_{1,k} & -b_{3/2,k} & 0 & 0 & \ldots & 0 \\
-b_{3/2,k} & 1 + B_{2,k} & -b_{5/2,k} & 0 & \ldots & 0 \\
0 & -b_{5/2,k} & 1 + B_{3,k} & -b_{7/2,k} & \ldots & 0 \\
\vdots & & \ddots & \ddots & \ddots & -b_{J_m-1/2,k} \\
0 & 0 & 0 & 0 & -b_{J_m-1/2,k} & 1 + B_{J_m,k}
\end{pmatrix} ,
$$

(3.59)

revealing that the dimension of each matrix $\mathbb{M}_k$ is $J_m \times J_m = (J-1) \times (J-1)$. With these definitions the recurrence relation (3.55) can be brought into the compact form

$$
\mathbb{T} \cdot \mathbf{w}^{n+1/2} + \mathbf{B}^{n+1/2} = \mathbf{R}^n ,
$$

(3.60)

where the vector $\mathbf{B}^{n+1/2}$ contains the boundary values at $t = t^{n+1/2}$ and is given by

$$
\mathbf{B}^{n+1/2} = \begin{pmatrix}
-b_{1/2,1}\, \theta_{0,1}^{n+1/2} \\
0 \\
\vdots \\
0 \\
-b_{J_m+1/2,1}\, \theta_{J_m+1,1}^{n+1/2} \\
\vdots \\
-b_{1/2,K_m}\, \theta_{0,K_m}^{n+1/2} \\
0 \\
\vdots \\
0 \\
-b_{J_m+1/2,K_m}\, \theta_{J_m+1,K_m}^{n+1/2}
\end{pmatrix} ,
$$

(3.61)

while the i-th componente of the rhs vector $\mathbf{R}^n$ (cf. (3.55)) at the time level $t = t^n$ reads as:

$$
\forall i; \quad i = J_m\,(k-1) + j \quad :
$$
$$
R_i^n \;=\; \frac{c_{j,k-1/2}}{r_k}\, \theta_{j,k-1}^n + \left(1 - C_{j,k}\right) \theta_{j,k}^n
$$
$$
+ \;\frac{c_{j,k+1/2}}{r_k}\, \theta_{j,k+1}^n + \frac{\Delta t}{2}\, \left[P_{eff}\right]_{j,k}^n ,
$$

(3.62)

where $j = 1, \ldots, J_m = J - 1$ and $k = 1, \ldots, K_m = K - 1$. In order to obtain the matrix-vector form of (3.56), we can proceed very similar as yet outlined for the relation (3.55). The variable vector at the time $t = t^{n+1}$ reads now as

$$
\mathbf{w}^{n+1} = \left(\theta_{1,1}^{n+1}, \ldots, \theta_{1,K_m}^{n+1}; \ldots; \theta_{J_m,1}^{n+1}, \ldots, \theta_{J_m,K_m}^{n+1}\right)^T ,
$$

(3.63)

where the second index runs fastest. The corresponding tridiagonal matrix $\tilde{\mathbb{T}}$ has the same structure as the matrix $\mathbb{T}$ given by (3.58). However, $\tilde{\mathbb{T}}$ is built up by

14

$J_m = J - 1$ block matrices. The shape of each block matrix is specified by

$$
\tilde{\mathbb{M}}_j = \begin{pmatrix}
1 + C_{j,1} & -\frac{c_{j,3/2}}{r_1} & 0 & 0 & \cdots & 0 \\
-\frac{c_{j,3/2}}{r_2} & 1 + C_{j,2} & -\frac{c_{j,5/2}}{r_2} & 0 & \cdots & 0 \\
0 & -\frac{c_{j,5/2}}{r_3} & 1 + C_{j,3} & -\frac{c_{j,7/2}}{r_3} & \cdots & 0 \\
\vdots & & \ddots & \ddots & \ddots & -\frac{c_{j,K_m-1/2}}{r_{K_m-1}} \\
0 & 0 & 0 & 0 & -\frac{c_{j,K_m-1/2}}{r_{K_m}} & 1 + C_{j,K_m}
\end{pmatrix} ,
\tag{3.64}
$$

from which it is obvious that the bock size is $K_m \times K_m$. The boundary values at the time level $t = t^{n+1}$ are elements of the vector $\mathbf{B}^{n+1}$ given by

$$
\mathbf{B}^{n+1} = \begin{pmatrix}
-\frac{c_{1,1/2}}{r_1} \theta_{1,0}^{n+1} \\
0 \\
\vdots \\
0 \\
-\frac{c_{1,K_m+1/2}}{r_{K_m}} \theta_{1,K_m+1}^{n+1} \\
\vdots \\
-\frac{c_{J_m,1/2}}{r_1} \theta_{J_m,0}^{n+1} \\
0 \\
\vdots \\
0 \\
-\frac{c_{J_m,K_m+1/2}}{r_{K_m}} \theta_{J_m,K_m+1}^{n+1}
\end{pmatrix} .
\tag{3.65}
$$

Furthermore, the i-th component of the vector $\mathbf{R}^{n+1/2}$ reads as

$$
\forall i; \quad i = K_m(j-1) + k \quad :
$$
$$
\begin{aligned}
R_i^{n+1/2} &= b_{j-1/2,k}\, \theta_{j-1,k}^{n+1/2} + \left(1 - B_{j,k}\right) \theta_{j,k}^{n+1/2} \\
&\quad + b_{j+1/2,k}\, \theta_{j+1,k}^{n+1/2} + \frac{\Delta t}{2} \left[P_{eff} \right]_{j,k}^{n+1/2} ,
\end{aligned}
\tag{3.66}
$$

for $k = 1, \ldots, K_m$ and $j = 1, \ldots, J_m$, and contains the complete rhs information at $t = t^{n+1/2}$. Finally, putting all formulas together, we obtain the compact matrix-vector notation of the recurrence relation (3.56)

$$
\tilde{\mathbb{T}} \cdot \mathbf{w}^{n+1} + \mathbf{B}^{n+1} = \mathbf{R}^{n+1/2} ,
\tag{3.67}
$$

which represents the updating prescription for the unknowns $\theta_{j,k}^{n+1}$ at the new time level $t = t^{n+1}$. It is clear from the relations (3.60) and (3.67), that we have to solve at each time step Δt two systems of coupled linear equations. Since the shape of the corresponding matrices $\mathbb{T}$ and $\tilde{\mathbb{T}}$ is tridiagonal, we can apply powerful numerical standard tools (see, e.g. [11]) to solve the occuring linear equations in a very effective manner.

As already mentioned, the Cartesian situation can be treated very similar to the presented cylinder symmetric case by setting the ratios $\frac{r_{k+1/2}}{r_k}$ and $\frac{r_{k-1/2}}{r_k}$ equal to one in the above given formulas.

3.2.3. *SOME REMARKS ON THE STABILITY OF THE SCHEMES.* In the following we are interested in the stability of the schemes proposed above. For that purpose, we consider the model equation for Cartesian coordinates without an external source given by

$$\frac{\partial \theta}{\partial t} = S_1 \frac{\partial^2 \theta}{\partial x^2} + S_2 \frac{\partial^2 \theta}{\partial y^2} \,, \tag{3.68}$$

where the physical fluxes (2.11) and (2.12) are already inserted under the assumption that the reduced conductivities (2.13) are independent of the spatial coordinates and the temperature. An explicit as well as implicit discretisation approach of this model is then investigated by applying the local stability analysis proposed by von Neumann. The eigenmode solutions of the difference equations are of the form

$$\theta_{j,k}^n = \xi^n \, e^{i\lambda \Delta x j} \, e^{i\mu \Delta y k} \,, \tag{3.69}$$

where the spatial wave numbers λ and μ are real numbers and $\xi^n = \xi^n(\lambda, \mu)$ denotes the amplification factor, which is, in general, a complex quantity that depends on these wave numbers. If the modulus of this amplification is greater than one for all λ and μ then the scheme is called unconditionally unstable. Otherwise, if $|\xi| \leq 1$ for any time step size Δt, then the scheme possesses the property of being unconditionally stable. For a more extended discussion of descriptive treatment of stability we refer, for instance, to the book of Smith [17].

EXPLICIT SCHEME:
Applying a modified Euler integration method in combination with a central **FD** approach for the spatial coordinates, the explicit scheme of the model equation (3.68) reads as

$$\tilde{\theta}_{j,k}^{n+1} = \theta_{j,k}^n + \alpha_1 \left[\theta_{j+1,k}^n - 2\theta_{j,k}^n + \theta_{j-1,k}^n \right] + \alpha_2 \left[\theta_{j,k+1}^n - 2\theta_{j,k}^n + \theta_{j,k-1}^n \right] \tag{3.70}$$

and

$$\begin{aligned} \theta_{j,k}^{n+1} &= \theta_{j,k}^n + \frac{\alpha_1}{2} \left[\left(\theta_{j+1,k}^n - 2\theta_{j,k}^n + \theta_{j-1,k}^n \right) + \left(\tilde{\theta}_{j+1,k}^{n+1} - 2\tilde{\theta}_{j,k}^{n+1} + \tilde{\theta}_{j-1,k}^{n+1} \right) \right] \\ &+ \frac{\alpha_2}{2} \left[\left(\theta_{j,k+1}^n - 2\theta_{j,k}^n + \theta_{j,k-1}^n \right) + \left(\tilde{\theta}_{j,k+1}^{n+1} - 2\tilde{\theta}_{j,k}^{n+1} + \tilde{\theta}_{j,k-1}^{n+1} \right) , \right] \end{aligned} \tag{3.71}$$

where the abbreviations

$$\alpha_1 = \frac{S_1 \, \Delta t}{(\Delta x)^2} \quad \text{and} \quad \alpha_2 = \frac{S_2 \, \Delta t}{(\Delta y)^2} \tag{3.72}$$

are used. Inserting the eigenmodes (3.69) into equation (3.70), we immediately obtain that

$$\tilde{\theta}_{j,k}^{n+1} = \theta_{j,k}^n \, Z \tag{3.73}$$

with

$$Z = 1 - 4\,\alpha_1 \, \sin^2\!\left(\frac{\lambda}{2}\Delta x\right) - 4\,\alpha_2 \, \sin^2\!\left(\frac{\mu}{2}\Delta y\right) . \tag{3.74}$$

Reformulating equation (3.71) with the relation (3.73) and the ansatz (3.69) and performing some algebra, we finally get

$$\xi = \frac{1}{2} \left(1 + Z^2 \right) , \tag{3.75}$$

which is the desired equation for the amplification factor of the modified Euler scheme. The stability of this scheme is guaranteed if $|\xi| \leq 1$ holds, which results

with the latter equation in the condition $Z^2 \leq 1$ for the expression specified by relation (3.74). A quick calculation then yields

$$2\,\Delta t \left[\frac{S_1}{(\Delta x)^2} \sin^2\left(\frac{\lambda}{2}\Delta x\right) + \frac{S_2}{(\Delta y)^2} \sin^2\left(\frac{\mu}{2}\Delta y\right) \right] \leq 1 \ , \tag{3.76}$$

which is the CFL stability criterion for the time step size Δt (see, e.g., [11]). For small Δx and Δy, equal thermal conductivities $S = S_1 = S_2$ and the abbreviation $\Delta^2 = \min\left[(\Delta x)^2,\ (\Delta y)^2\right]$ this condition reads as

$$\frac{2\,S\,\Delta t}{\Delta^2} \leq 1 \ . \tag{3.77}$$

In our numerical studies we allow that the conductivities may also depend on the temperature and, consequently, on the spatial location. Hence, we apply for our purposes the heuristic stability criterion

$$\Delta t \leq \frac{\sigma}{2\,\omega} \tag{3.78}$$

with

$$\omega = \max_{\forall j,k} \left[\frac{(S_1)_{j,k}}{(\Delta x)^2} + \frac{(S_2)_{j,k}}{(\Delta y)^2} \right] \ , \tag{3.79}$$

where σ denotes the Courant number, which has to be selected according to $0 < \sigma < 1$. Obviously, this stability condition have to be calculated in each temporal iteration cycle.

Finally we note that there are unconditionally stable explicit schemes – for example, the DuFort-Frankel approach –, which converge for any Δt (see, for instance, [12]).

IMPLICIT SCHEME:

The implicit scheme of the model equation (3.68) is obtained by using the above introduced ADI method and reads as

$$\theta_{j,k}^{n+1/2} - \frac{\alpha_1}{2}\left[\theta_{j+1,k}^{n+1/2} - 2\theta_{j,k}^{n+1/2} + \theta_{j-1,k}^{n+1/2}\right] = \theta_{j,k}^{n} + \frac{\alpha_2}{2}\left[\theta_{j,k+1}^{n} - 2\theta_{j,k}^{n} + \theta_{j,k+1}^{n}\right] \tag{3.80}$$

and

$$\theta_{j,k}^{n+1} - \frac{\alpha_2}{2}\left[\theta_{j,k+1}^{n+1} - 2\theta_{j,k}^{n+1} + \theta_{j,k-1}^{n+1}\right] = \theta_{j,k}^{n+1/2} + \frac{\alpha_1}{2}\left[\theta_{j+1,k}^{n+1/2} - 2\theta_{j,k}^{n+1/2} + \theta_{j-1,k}^{n+1/2}\right] \ , \tag{3.81}$$

where the abbreviations α_1 and α_2 are already specified by the relations (3.72). With the eigenmodes given by the ansatz (3.69), the first-step difference equations (3.80) yields the equation

$$\xi^{1/2} = \frac{1 - 2\,\alpha_2\,\sin^2\left(\frac{\mu}{2}\Delta y\right)}{1 + 2\,\alpha_1\,\sin^2\left(\frac{\lambda}{2}\Delta x\right)} \tag{3.82}$$

for the amplification factor. With the definitions (3.72) in mind it is obvious, that the stability criterion $|\xi| \leq 1$ in this step of the ADI approach is fulfiled for any size Δt. Inserting once again the eigenmode solution (3.69) into the second-step equation (3.81) and using the result (3.82) of the first-step equation, we get for the amplification factor of the full time step Δt the expression (cf., [12])

$$\xi = \frac{1 - 2\,\alpha_2\,\sin^2\left(\frac{\mu}{2}\Delta y\right)}{1 + 2\,\alpha_1\,\sin^2\left(\frac{\lambda}{2}\Delta x\right)} \cdot \frac{1 - 2\,\alpha_1\,\sin^2\left(\frac{\lambda}{2}\Delta x\right)}{1 + 2\,\alpha_2\,\sin^2\left(\frac{\mu}{2}\Delta y\right)}\;. \qquad (3.83)$$

This result reveals that the stability condition $|\xi| \leq 1$ is satisfied for any time step size Δt and, consequently, the ADI differencing scheme is unconditionally stable. However, in the case where the thermal conductivities are not independent of temperature the unconditional stability may be lost. The reason for this behavior of the scheme can be attributed to the occurence of nonlinear instabilities, which could not be investigated within the framework of the considered linear analysis. Clearly, in the context of such situation we have to estimate carefully the temporal discretisation size.

4. NUMERICAL RESULTS

In oder to demonstrate the quality and property of the introduced approximation methods for the diffusion equation in two-dimensional space, we discuss numerical experiments where the numerical solution procedure is applied in different situations. First, simulation results for exactly solvable model problems are presented in this section, which reveal that the implementation of the proposed schemes produces accurate approximations and runs in a very reliable manner. In a separate section the approximation techniques are applied to a more practical problem, namely, the diamond disc window [16].

In the following we present direct comparisons between numerically computed and the exact solutions. Then, in order to investigate the global approximation behavior of the proposed numerical schemes more closely, we consider for problems with an exact solution $u(\mathbf{x}, t)$ the L_2-error norm. This relative discrete L_2-error norm is defined by

$$\frac{\|\theta(\mathbf{x}, t) - u(\mathbf{x}, t)\|_{L_2}}{\|u(\mathbf{x}, t)\|_{L_2}} = \sqrt{\frac{\sum_{j,k}\left[\theta_{j,k}(t) - u(x_j, y_k, t)\right]^2 \Delta x_j\,\Delta y_k}{\sum_{j,k}\left[u(x_j, y_k, t)\right]^2 \Delta x_j\,\Delta y_k}}\;, \qquad (4.1)$$

and computed for different grids with increasing refinement. In this formula, $\theta_{j,k}(t)$ denotes the approximation of the conservation equation (2.1) and $u(x_j, y_k, t)$ is the exact solution of the diffusion problem at the coordinate points (x_j, y_k) at time t. Especially, the temporal evolution of the quantity $\frac{\|\theta(\mathbf{x},t) - u(\mathbf{x},t)\|_{L_2}}{\|u(\mathbf{x},t)\|_{L_2}}$ contains information about the global approximation error of the spatial dicretisation.

4.1. **A two-dimensional rotationally symmetric problem.** In the following we consider the computational domain $\Omega = [0, 3/2] \times [3, 0]$ in the (z, r)-plain with the property of rotational symmetry with respect to the z-axis. The parabolic diffusion problem is specified by equation (2.10) with the heat fluxes

$$F \;=\; \frac{1}{18\pi^2}\frac{\partial\theta}{\partial z}\;, \qquad (4.2)$$

$$G \;=\; \frac{1}{2}\frac{\partial\theta}{\partial r}\;, \qquad (4.3)$$

18

and the source term

$$P_{eff} = \cos(3\pi z)\, J_0(r) \qquad (4.4)$$

for all $(z,\, r) \in \Omega$ and all $t > 0$. The analytical solution of this problem is given by

$$u(z, r, t) = \sin(3\pi z)\, J_0(r)\, e^{-t} + \cos(3\pi z)\, J_0(r)\,, \qquad (4.5)$$

where $J_0(r)$ denotes the zeroth order Bessel function of the first kind. We remark that the analytical solution (4.5) also satisfies the conservation equation (2.15) at the symmetry axis $r = 0$: this becomes obvious by inserting (4.5) into this equation and performing subsequently the limit $r \to 0$. From the exact result (4.5), we immediately obtain the necessary initial data

$$u_0(z, r) = \left[\sin(3\pi z) + \cos(3\pi z)\right] J_0(r)\,, \qquad (4.6)$$

as well as the boundary conditions

$$
\begin{aligned}
g_1(r, t) &= u(0, r, t) = J_0(r)\,, \\
g_2(r, t) &= u(3/2, r, t) = J_0(r)\, e^{-t}\,, \\
h_1(z_j, t) &= \theta_{j,1}(t)\,, \quad \forall j\,, \\
h_2(z, t) &= u(z, 3, t) = J_0(3)\left[\sin(3\pi z)\, e^{-t} + \cos(3\pi z)\right]\,, \qquad (4.7)
\end{aligned}
$$

which obviously depends on space and time and are seen in Figure 4.1 for $t = 1$ and $t = 4$. To study especially the global approximation properties, the numerical experiments are furthermore performed on three different grid arrangements composed, respectively, by 15×30 (G1), 30×60 (G2) and 60×120 (G3) discretisation nodes of the domain Ω. The temporal evolution of the diffusion is recorded up to $t = 4$, which correspond to 4000 iteration cycles for the default time step size $\Delta t = 10^{-3}$. An overview of the numerical (colored contours) and exact (solid lines) solution on the domain Ω discretised by G2 for the initial (4.6) and boundary (4.7) is given in Figure 4.2. There, the temporal evolution of the temperature θ is recorded at the times $t = 0.5$ (upper) and $t = 2.0$ (lower plot), corresponding to 500 and 2000 iterations in time. A closer inspection of both snapshots reveals a very good agreement of the general features of the numerically and analytically computed solution. More quantitative comparisons between the numerical and analytical solutions are depicted in Figure 4.3, which obviously demonstrates the quality and ability of the applied approximation techniques. There, slices parallel to the z ($r_0 = 1.2$) and r ($z_0 = 0.75$) axis are shown for the temperture θ. Clearly, the exact values are reproduced very well by the numerical approximation. The explicit temporal computations presented in the Figure 4.2 and Figure 4.3 are performed with the classical fourth-order accurate Runge-Kutta approximation technique (cf., Section 3.2.1).

The relative discrete L_2-error norm defined by the expression (4.1) is an appropriate and evident measure to check the behavior of the numerical scheme more closely. In Figure 4.4 the approximation results measured by (4.1) for the computational grid G1, G2 and G3 are plotted with respect to time. Obviously, the values obtained with the classical Runge-Kutta scheme (solid lines) and the modified Euler technique (open symbols) are nearly identical. Furthermore, these results reveal that the discrete L_2-error is reduced by a factor of four (≈ 3.9) when switching from
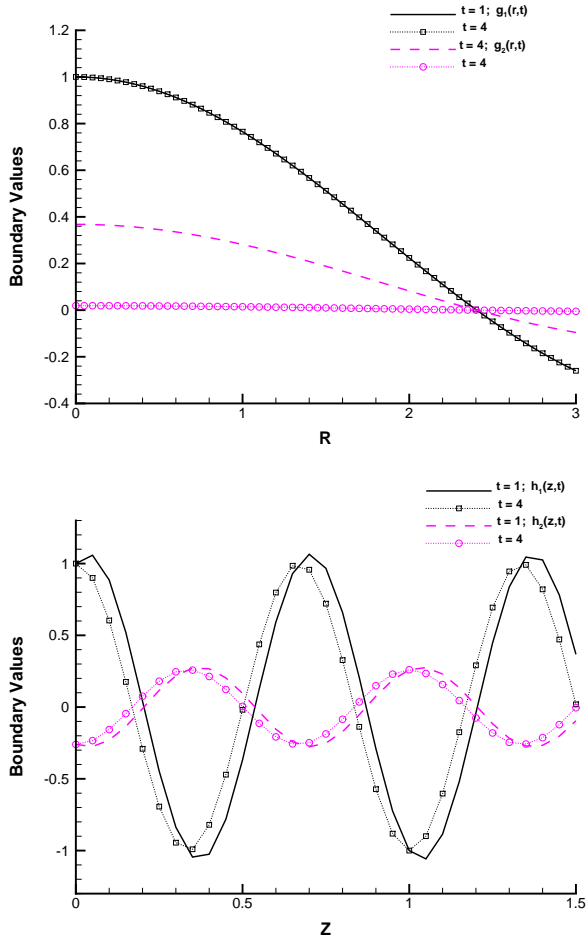
19

FIGURE 4.1. Space and time-dependent boundary conditions recorded at $t = 1$ and $t = 4$. Upper plot: left and right functions $g_1(r, t)$ and $g_2(r, t)$. Lower plot: lower and upper functions $h_1(z, t)$ and $h_2(z, t)$ (cf., Figure 2.1). Discretisation is established by the 30×60 grid (G2) and the time step size $\Delta t = 10^{-3}$.

grid G1 to grid G2 and once again a factor of four (≈ 3.9) taking grid G3 instead G2 for the computation. From this observation we can compute the experimental order of convergence (EOC) for the scheme, which is defined by

$$\mathsf{E}OC = \frac{1}{\ln(2)} \ln \left[\frac{\|\theta^h(\mathbf{x}, t) - u(\mathbf{x}, t)\|_{L_2}}{\|\theta^{2h}(\mathbf{x}, t) - u(\mathbf{x}, t)\|_{L_2}} \right], \tag{4.8}$$

where $u(\mathbf{x}, t)$ is the exact solution and $\theta^h(\mathbf{x}, t)$ and $\theta^{2h}(\mathbf{x}, t)$ denotes the numerical result with a minimal spacing of h and $2h$, respectively. Consequently, the results calculated with (4.8) indicates that the proposed explicit FD scheme has an averaged experimental order of convergence of about 1.95. A comparison between an explicit Heun scheme (cf., equations (3.43) and (3.44)) and the implicit operator splitting approach (cf., equations (3.60) and (3.67)) is depicted in Figure 4.5, where the
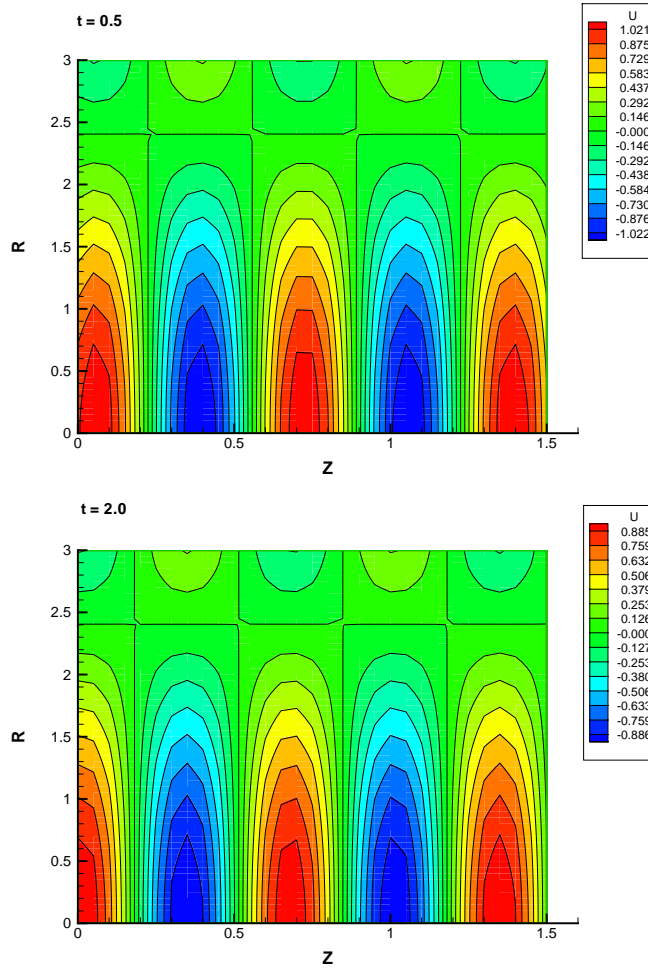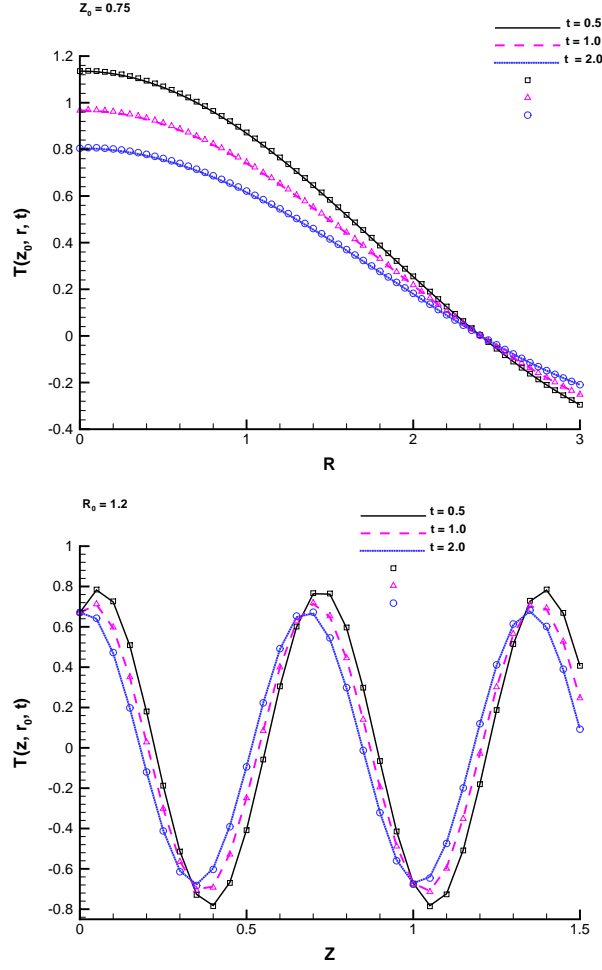
FIGURE 4.2. Comparison between the numerical (colored contours) and the exact (solid lines) solution. The plots are recorded at $t = 0.5$ (upper) and $t = 2.0$ (lower picture). Discretisation is established by the 30×60 grid (G2) and the time step size $\Delta t = 10^{-3}$.

discrete L_2 error norm (cf., relation (4.1)) is plotted for the grid G2 (upper) and G3 (lower curves). It is obvious from this figure, that the values from the implicit method (open symbols) are − nearly all − on those computed with the explicit technique (solid and dashed lines). Hence, we conclude that the experimental order of convergence of the implicit scheme is the same as for the explicit method, namely, about 1.95.

4.2. **A two-dimensional Cartesian Problem.** For the sake of completness, we present in the following a numerical experiment which is performed on the computational domain $\Omega = [3/2, 0] \times [2, 0]$ in the (x, y)-plain. The diffusion problem for Cartesian coordinates is similar defined to those one described by equation (2.10)

FIGURE 4.3. Comparison between the numerical (open symbols) and the exact (solid lines) solution. The slices are recorded at $z_0 = 0.75$ (upper) and $r_0 = 1.2$ (lower picture) for the times $t = 0.5$, $t = 1.0$ and $t = 2.0$. Discretisation is established by the 30×60 grid (G2) and the time step size $\Delta t = 10^{-3}$.

and reads as

$$\frac{\partial \theta}{\partial t} = \frac{\partial F}{\partial x} + \frac{\partial G}{\partial y} + P_{eff}(\mathbf{x}, t; \theta) \ , \qquad (4.9)$$

where the fluxes and the source term are given by

$$F \quad = \quad S_1(\mathbf{x}; \theta) \, \frac{\partial \theta}{\partial x} = \frac{1}{18\pi^2} \frac{\partial \theta}{\partial x} \ , \qquad (4.10)$$

$$G \quad = \quad S_2(\mathbf{x}; \theta) \, \frac{\partial \theta}{\partial y} = \frac{1}{2\pi^2} \frac{\partial \theta}{\partial y} \ , \qquad (4.11)$$

and

$$P_{eff} = 2 \cos(3\sqrt{2}\pi x) \, \cos(\sqrt{2}\pi y) \ , \qquad (4.12)$$

respectively. It is an easy exercise to proof that

$$u(x, y, t) = \sin(3\pi x) \, \cos(\pi y) \, e^{-t} + \cos(3\sqrt{2}\pi x) \, \cos(\sqrt{2}\pi y) \qquad (4.13)$$

22
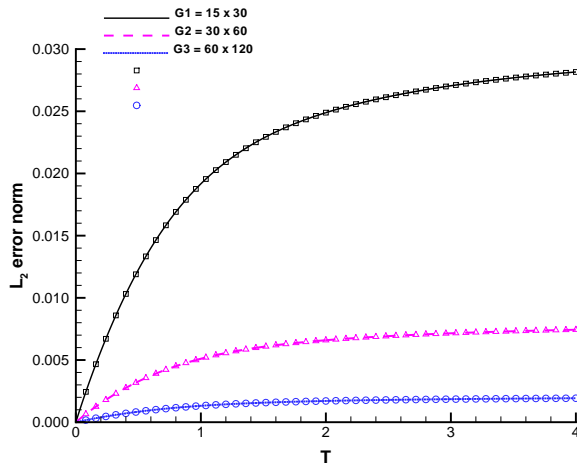
FIGURE 4.4. Relative dicrete L_2-error norm (4.1) computed for the meshes G1=15 × 30 (solid), G2=30 × 60 (dashed) and G3=60 × 120 (dotted line) with a classical Runge-Kutta (lines) and a modified Euler (open symbols) scheme. For these computations the time step size was fixed equal to $\Delta t = 4 \cdot 10^{-4}$.
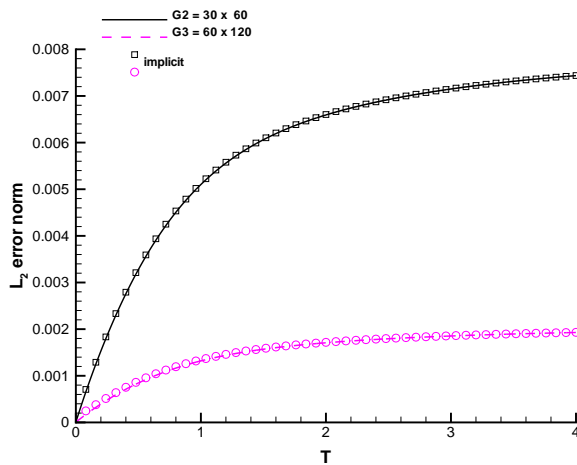
FIGURE 4.5. Relative dicrete L_2-error norm (4.1) computed for the meshes G2=30 × 60 (upper) and G3=60 × 120 (lower curves) with an explicit Heun scheme (solid and dashed lines) and an implicit operator splitting method (open symbols). The time step size was fixed equal to $\Delta t = 4 \cdot 10^{-4}$ and $\Delta t = 10^{-3}$ for the explicit and implicit computations, respectively.

is the analytical solution of the posed diffusion problem. This exact result is then taken to fix the for numerical calculations important initial values

$$u_0(x,y) = \sin(3\pi x) \cos(\pi y) + \cos(3\sqrt{2}\pi x) \cos(\sqrt{2}\pi y) \tag{4.14}$$

23

and the necessary boundary datas

$$
\begin{aligned}
g_1(y,t) &= u(0,y,t) = \cos(\sqrt{2}\pi y) \,, \\
g_2(y,t) &= u(3/2,y,t) = \cos(\pi y)\,e^{-t} + \cos(\frac{9\sqrt{2}}{2}\pi)\,\cos(\sqrt{2}\pi y) \,, \\
h_1(x,t) &= u(x,0,t) = \sin(3\pi x)\,e^{-t} + \cos(3\sqrt{2}\pi x) \,, \\
h_2(x,t) &= u(x,2,t) = \sin(3\pi x)\,e^{-t} + \cos(3\sqrt{2}\pi x)\,\cos(2\sqrt{2}\pi) \,. \qquad (4.15)
\end{aligned}
$$

These time and space dependent boundary conditions are depicted in Figure 4.6 for $t = 1$ and $t = 4$. The temporal evolution of the considered diffusion problem is
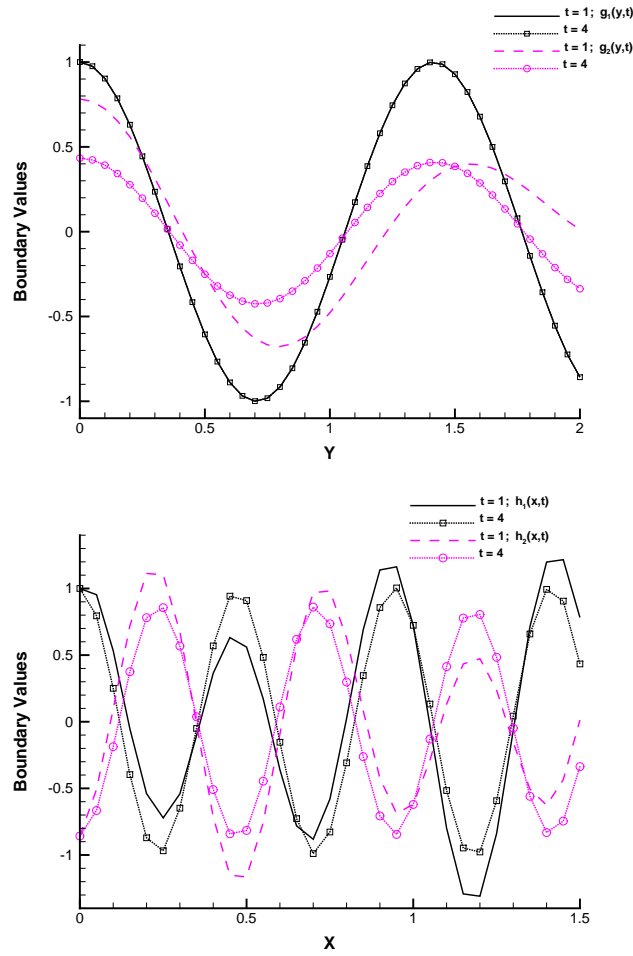
FIGURE 4.6. Space and time-dependent boundary conditions recorded at $t = 1$ and $t = 4$. Upper plot: left and right functions $g_1(y,t)$ and $g_2(y,t)$. Lower plot: lower and upper functions $h_1(x,t)$ and $h_2(x,t)$. Discretisation is established by the 30×40 grid (G2) and the time step size $\Delta t = 8 \cdot 10^{-3}$.

propagated up to $t = 4$, which is equivalent to 500 temporal iteration cycles with a time step size of $\Delta t = 8 \cdot 10^{-3}$. Most results discussed in the following are obtained

24

with the alternating-direction implicit method introduced in Section 3.2.2, which is second-order accurate in both space and time and known to be very stable. To
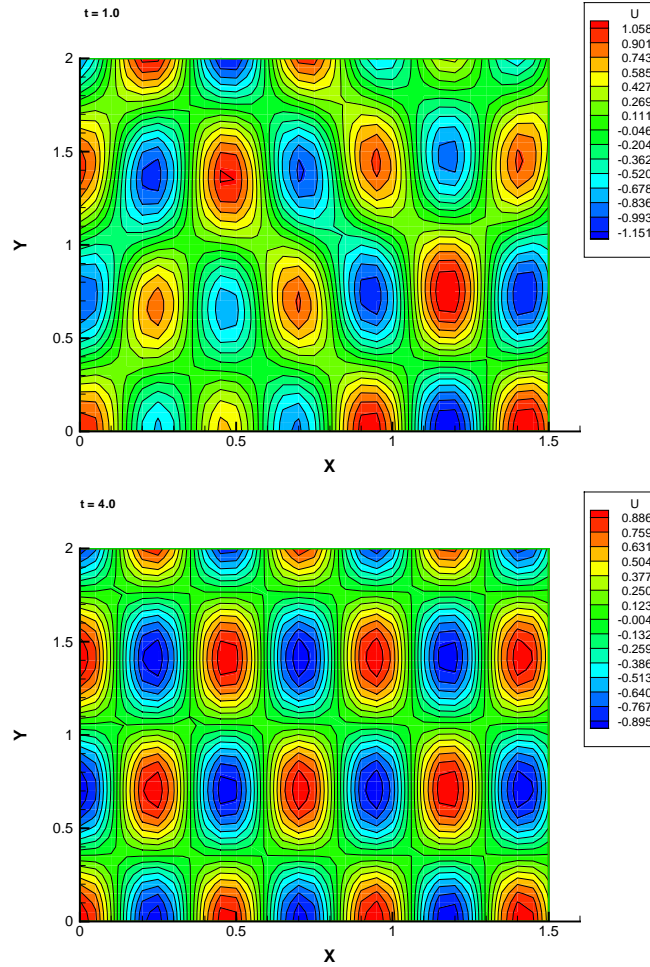

FIGURE 4.7. Comparison between the numerical (colored contours) and the exact (solid lines) solution. The plots are recorded at $t = 1.0$ (upper) and $t = 4.0$ (lower picture). Discretisation is established by the 30 × 40 grid (G2) and the time step size $\Delta t = 8 \cdot 10^{-3}$.

get an impression of the shape of the solution, the numerical (colored contours) and analytical (solid lines) results at the times $t = 1$ and $t = 4$ are presented in Figure 4.7 for the computational grid $\mathsf{G2} = 30 \times 40$. A closer inspection of these two snapshots indicates, that we can expect an excellent agreement between numerical and analytical calculated values. A more direct comparison of the numerically obtained and the exactly computed data is given in Figure 4.8, where slices parallel to the x ($y_0 = 0.8$) and y ($x_0 = 0.75$) axis are seen. Clearly, these two plots convince us from the quality of the used numerical approximations: The numerical values obtained with the operator splitting implementation reproduce very well the analytical data. In order to investigate the global approximation properties of the
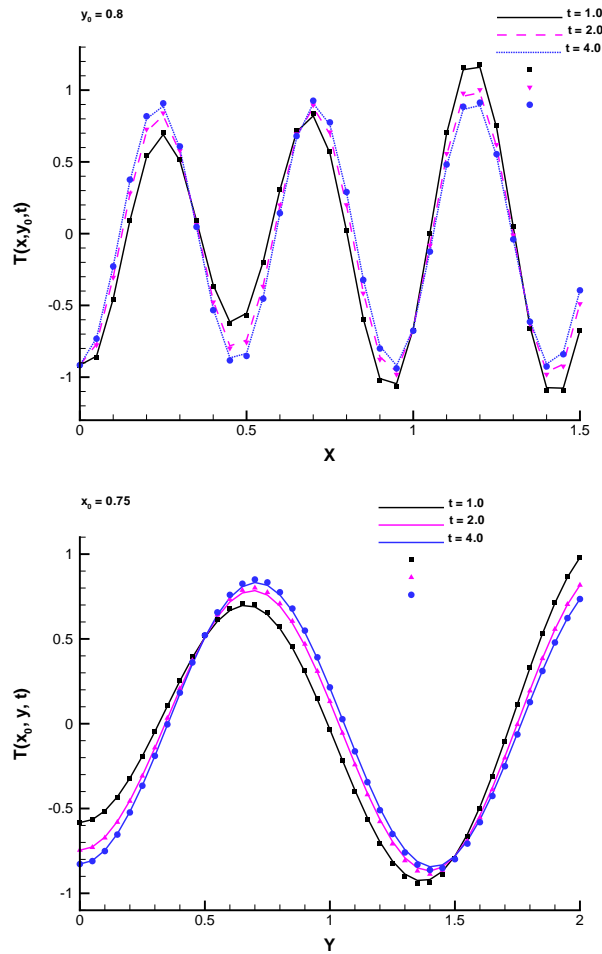
FIGURE 4.8. Comparison between the numerical (symbols) and the exact (solid lines) solution. The slices are recorded at $y_0 = 0.8$ (upper) and $x_0 = 0.75$ (lower picture) for the times $t = 1.0$, $t = 2.0$ and $t = 4.0$. Discretisation is established by the 30×40 grid (G2) and the time step size $\Delta t = 8 \cdot 10^{-3}$.

introduced implicit approach, numerical studies are performed on two further grids discretising the domain Ω by 15×20 (G1) and 60×80 (G3) nodes. The measure to check the behavior of the applied implicit approximation technique more closely, is given by the relative discrete L_2-error norm explained by equation (4.1). The temporal evolution of the L_2-error norm computed for the three computational meshes G1, G2 and G3 is seen in in Figure 4.9. An estimation with equation (4.8) indicates that the averaged experimental order of convergence is of about 2.08 for the proposed implicit approach. A comparison of the discrete L_2-error for the grid G2 (upper) and G3 (lower curves) computed with the implicit operator splitting (solid and dashed lines) and the explicit Runge-Kutta (open symbols) technique is given in Figure 4.10. It is obvious from this plot that the long-time behavior (which corresponds to the equilibrium solution) of both approaches is
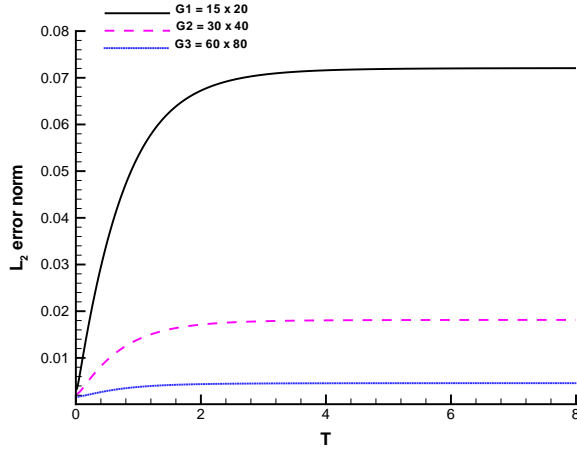
FIGURE 4.9. Relative dicrete L_2-error norm (4.1) computed for the meshes G1=15×20 (solid), G2=30×40 (dashed) and G3=60×80 (dotted line) with the implicit operator spliting scheme. For these computations the time step size was fixed equal to $\Delta t = 8 \cdot 10^{-3}$.
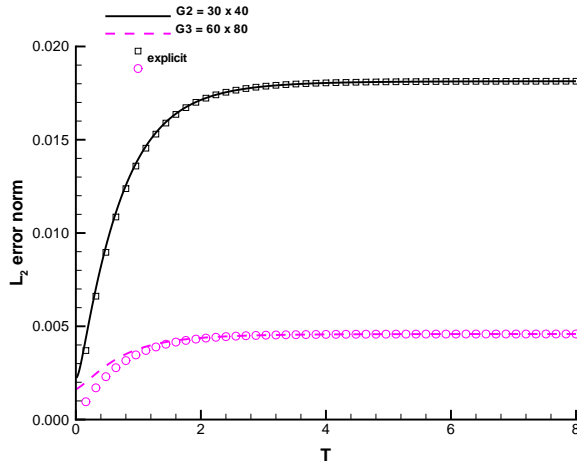

FIGURE 4.10. Relative dicrete L_2-error norm (4.1) computed for the meshes G2=30×40 (upper) and G3=60×80 (lower curves) with an explicit Runge-Kutta scheme (open symbols) and an implicit operator splitting method (solid and dashed lines). The time step size was fixed equal to $\Delta t = 4 \cdot 10^{-3}$ and $\Delta t = 8 \cdot 10^{-3}$ for the explicit and implicit computations, respectively.

nearly identical. However, in the short-time regime the approximation property of the explicit method is better than those obtained with the implicit scheme. This observation is expected, since the details of the small-scale evolution from the initial data with the implicit scheme are less accurate for larger time step size Δt.

5. SIMULATION OF A SYNTHETIC DIAMOND DISC WINDOW

In this section the basic physical quantities, which are important to simulate numerically the main features of the heat transfer problem in the context of a diamond disc window are introduced. A sketch of the computational domain Ω of such a diamond window is seen in Figure 2.1 and the corresponding typical geometrical measurements are listed in Table 5.1. Additional, for some physical quantities of this diamond window it is possible to establish empirical relations in parametrised form to model the observed physical behavior accucately, which are then highly efficient for numerical computations.

5.1. **The local effective power density.** The effective power density p_{eff}, which locally couples to the considered medium, is composed by different physical contributions and is, in general, defined by

$$p_{eff}(\mathbf{x}, t; \theta) := \frac{d\Pi_{eff}(\mathbf{x}, t; \theta)}{dV} , \tag{5.1}$$

where Π_{eff} denotes the effective power measured in $[\Pi_{eff}] = W$. In the following the essential contributions to the effective power change $d\Pi_{eff}$ are briefly reviewed.

5.1.1. *POWER ABSORPTION.* This kind of power deposition is based, in general, on a volumetric heating mechanism. In the context of the present investigations we consider a thin medium with thickness D and use the simplified ansatz

$$d\Pi_{abs}(\mathbf{x}, t; \theta) = D^{-1} A P(\mathbf{x}) dV , \tag{5.2}$$

where $P(\mathbf{x})$ denotes the power distribution in $[P] = W/cm^2$ and A is the power absorption coefficient. This coefficient represents an approximation and is given by the formula [16]

$$A = \pi f (\epsilon + 1) \tan(\delta) \frac{D}{c} , \tag{5.3}$$

which is valid only for resonant thickness of the window and for $\tan(\delta) < 10^{-3}$ – for a more accurate expression of this coefficient we refer to [9]. Here, f, ϵ and $\tan(\delta)$ denote the frequency of the incident beam, the permittivity of the considered material (where the temperature dependence can be ignored) and the loss tangent of the medium , respectively, and $c = 2.99792 \cdot 10^{10} \ cm/s$ is the velocity of light in vacuum. Furthermore, in the present case the loss tangent may be parametrised by an expression of the form

$$\tan(\delta) = A_c f^p \theta^q , \tag{5.4}$$

where f is the frequency in GHz and A_c, p and q are constants which all depend on the material under consideration. Because the temperature dependence of the loss tangent is very weak, the parameter q is usually set equal to zero. The power distribution in the material can be modelled by the ansatz

$$P(\mathbf{x}) = P_{tot} \mathcal{D}(\mathbf{x}) , \tag{5.5}$$

where P_{tot} is the totally deposited power by the beam in the medium. For our purposes, we use as distribution function $\mathcal{D}(\mathbf{x})$ a Gaussian profile specified according to

$$\mathcal{D}(\mathbf{x}) = \frac{2}{\pi w^2} e^{-2\frac{r^2}{w^2}} , \tag{5.6}$$

where the parameter w denotes the so-called beam radius. Note that other power distribution functions $\mathcal{D}(\mathbf{x})$ can be handled equally well. We finally remark that the power density deposition due to absorption is simply given by $p_{abs} = \frac{d\Pi_{abs}}{dV} = D^{-1} A P(\mathbf{x})$. For the first attempt to simulate numerically a diamond disc window, we use for the mentioned parameters the values listed in Table 5.2.

5.1.2. *POWER LOSS BY CONDUCTION.* Consider the situation where some parts of the surface of interest $\partial\Omega$ are cooled by, for instance, water. The power change due to conduction through the surface element dA is obtained from the expression

$$d\Pi_{cond}(\mathbf{x}, t; \theta) = -\alpha_m \left(\theta - \theta_{cool}\right) dA , \qquad (5.7)$$

where θ_{cool} denotes the temperature of the cooling medium and α_m represents the heat transfer (or conduction) coefficient measured in $[\alpha_m] = W/cm^2/K$. The power density loss as a result of conduction is then given by $p_{cond} = \frac{d\Pi_{cond}}{dV} = -\alpha_m \left(\theta - \theta_{cool}\right) \frac{dA}{dV}$. For numerical purposes the two parameters occuring in relation (5.7) are fixed to values found in Table 5.2.

5.1.3. *POWER LOSS BY CONVECTION.* The change of heat loss rate at the surface of the material caused by convection may be modelled in a very simplified manner by the ansatz

$$d\Pi_{conv}(\mathbf{x}, t; \theta) = -\alpha_c \left(\theta - \theta_e\right) dA . \qquad (5.8)$$

Here, θ_e is the temperature of the enviroment and α_c denotes the convection heat transfer coefficient measured in units of $[\alpha_c] = W/cm^2/K$. The power density due to convection then reads as $p_{conv} = \frac{d\Pi_{conv}}{dV} = -\alpha_c \left(\theta - \theta_e\right) \frac{dA}{dV}$.

5.1.4. *POWER LOSS BY THERMAL RADIATION.* The power change as a consequence of grey, diffuse thermal radiation from the surface of the material is detemined by the equation [6, 18]

$$d\Pi_{rad}(\mathbf{x}, t; \theta) = -\sigma_B \, \epsilon(\theta) \left(\theta^4 - \theta_e^4\right) dA , \qquad (5.9)$$

where the Stefan-Boltzmann constant is given by $\sigma_B = 5.603 \cdot 10^{-12} \, W/cm^2/K^4$. Furtermore, θ_e again denotes the temperature of the enviroment and $\epsilon(\theta)$ is emissivity function of the material − also denoted as degree of blackness − which, in general, depends on the temperature. The resulting power density due to radiation is then obtained from $p_{rad} = \frac{d\Pi_{rad}}{dV} = -\sigma_B \, \epsilon(\theta) \left(\theta^4 - \theta_e^4\right) \frac{dA}{dV}$.

The source term of the diffusion problems given by (2.1), namely the effective local power density, can now be determined by applying definition (5.1) to the effective power change contributions which are given by

$$d\Pi_{eff} = \begin{cases} d\Pi_{abs} , & \text{for } \mathbf{x} \in \Omega \\ d\Pi_{abs} + d\Pi_{cond} + d\Pi_{conv} + d\Pi_{rad} , & \text{for } \mathbf{x} \in \partial\Omega \end{cases} . \qquad (5.10)$$

Neglecting for the moment the contribution given by convection and radiation, we obtain with (5.2) and (5.7) the expression

$$
p_{eff} = \begin{cases} D^{-1} A\, P(\mathbf{x})\, , & \text{for } \mathbf{x} \in \Omega \\ D^{-1} A\, P(\mathbf{x}) - \alpha_m \left(\theta - \theta_{cool} \right) \frac{dA}{dV}\, , & \text{for } \mathbf{x} \in \partial\Omega \end{cases} , \tag{5.11}
$$

for the effective local power density, which will be used as the source for the numerical experiments dicussed later in this section. It is obvious from the latter relation (5.11), that the effective applied power density in the interior of the domain is given by power absorption only, while at the border different power contributions may be important for accurate modelling of the diffusion process.

5.2. **Parameter law for the thermal conductivity.** It has been observed that the temperature dependence of the thermal conductivities can be expressed by a parametrised law, which reads as [16]

$$
\mathsf{s}_i(\mathbf{x}; \theta) = \mathsf{s}_{R,i} \left(\frac{\theta}{\theta_{R,i}} \right)^{-Z_i} \quad i = 1, 2 \, . \tag{5.12}
$$

Here, the reference thermal conductivities $\mathsf{s}_{R,i}$ and the reference temperatures $\theta_{R,i}$ as well as the exponents Z_i have to be well chosen for the materials under consideration. This special form of parametrisation has been proven to be valid for the diamond disc in the temperature range of $290\,K \leq \theta \leq 1000\,K$ but is not applicable at lower temperatures [16]. For the numerical investigations discussed below the values of these parameters are fixed and given in Table 5.2.

5.3. **Parametrisation of the specific heat.** The temperature-dependent behavior of the specific heat capacity may be modelled by the empirical relation

$$
C_p(\theta) = P_C\, e^{-Q/\theta} \, , \tag{5.13}
$$

where the parameters P_C and Q have to been selected carefully for each material of interest. It is obvious that these parameters are measured in units of $[P_C] = J/g/K$ and $[Q] = K$, respectively. If the temperature dependence can be neglected we find that $C_p(\theta) = P_C$ holds and, hence, P_C may be regarded as the reference specific heat. This situation is assumed for the numerical simulations presented below, for which both parameters are fixed according to the values listed in Table 5.2. We note furthermore that for the temperature-independent specific heat capacity and for the typical mass density of $\rho = 3.52 g/cm^3$ the expression explained by $\xi = \frac{1}{\rho C_p}$ (cf.,(2.9)) takes the value $\xi = 0.5463 \frac{cm^3 K}{Ws}$.

5.4. **Numerical diamond disc experiments.** In this section we present numerical results obtained from the diamond disc window simulation. The cylinder symmetrical computational domain Ω is schematically depicted at Figure 2.1 and the measurements of this domain is listed in Table 5.1.

Disc thickness	$D = 0.20$ cm
Disc radius	$R_0 = 4.40, \ldots, 5.00$ cm
Disc radius	$R_1 = 4.40$ cm
Aperture radius	$R_A = 4.00$ cm

Table 5.1: Geometrical parameters of the computational domain Ω depicted in Figure 2.1.

Frequency f	$f = 1.4 \cdot 10^{11}\, Hz$
Permittivity ϵ	$\epsilon = 5.67$
Loss tangent $\tan(\delta)$	$\tan(\delta) = 2.0 \cdot 10^{-5}$
Total power P_{tot}	$P_{tot} = 1.0 \cdot 10^6\, W$
Gaussian beam radius w	$w = 2.6\, cm$
Heat transfer coef. α_m	$\alpha_m = 1.2\, \frac{W}{cm^2 K}$
Cooling temperature θ_{cool}	$\theta_{cool} = 293\, K$
Mass density ρ	$\rho = 3.52\, \frac{g}{cm^3}$
Exponent Z	$Z_1 = Z_2 = 1.41$
Reference conductivity s_R	$s_{R,1} = s_{R,2} = 18 \frac{W}{cm\, K}$
Reference temperature θ_R	$\theta_{R,1} = \theta_{R,2} = 293\, K$
Reference specific heat P_C	$P_C = 0.52\, \frac{J}{g K}$
Reference temperature Q	$Q = 0\, K$

Table 5.2: Parameters used for modelling the power absorption, the heat transfer due to conduction, the thermal conductivity relation and the specific heat law.

In the following we describe a series of numerical experiments, where the physical parameters, summarised in the Tables 5.2, are the same for all calculations while the radius R_0 and the boundary conditions are changed. The initial conditions are fixed to

$$\theta_0(z_j, r_k) = 293.0 \text{ K}; \quad \forall j, k \tag{5.14}$$

in the course of all the numerical computations. Since the disc window is symmetrical with respect to the z-axis, the boundary function

$$h_1(z_j, t) = \theta_{j,1}(t) ; \quad \forall j , t \geq 0 , \tag{5.15}$$

already introduced above, has to be the same for all numerical computations.

EXPERIMENT 1:
For this numerical simulation the radius is fixed equal to $R_0 = 4.4$ cm. The boundary data on the left and right border of Ω are "thermally insulated surface" conditions and reads as

$$g_1(r_k, t) = \theta_{1,k}(t) ; \quad \forall k , t \geq 0 , \tag{5.16}$$

$$g_2(r_k, t) = \theta_{J-1,k}(t) ; \quad \forall k , t \geq 0 . \tag{5.17}$$

At the top boundary of the domain at $r = R_0$ a "surface cooling" condition is imposed, for which we obtain the expression (cf., equation (3.36))

$$h_2(z_j, t) = \theta_{j,K-1}(t) - \Delta r \frac{\alpha_m}{(\mathsf{s}_2)_{j,K-1}} \left[\theta_{j,K-1}(t) - \theta_{cool} \right] \qquad (5.18)$$

for the border updating, where s_2 and θ_{cool} are found in Table 5.2. The spatial
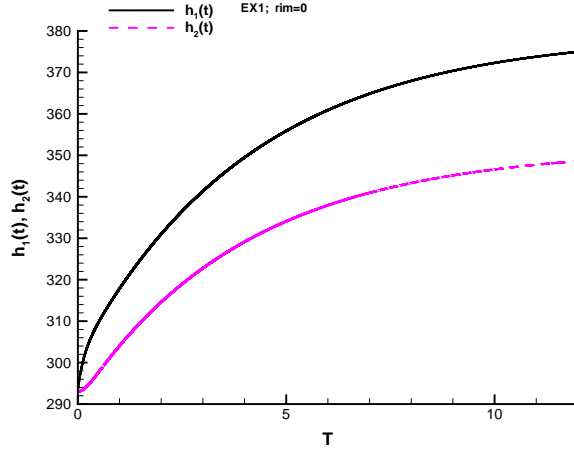
FIGURE 5.1. Bottom and top boundary functions $h_1(t)$ and $h_2(t)$ with respect to time (measured in seconds). The rim length is $r_{rim} = 0$ for this simulation.

domain is discretised by $J \times K = 13 \times 290$ nodes resulting in an equidistant spacing of $\Delta z = 0.0154$ cm and $\Delta r = 0.0152$ cm, which is retained for all further computations presented in the following. In Figure 5.1 the bottom (upper) and top
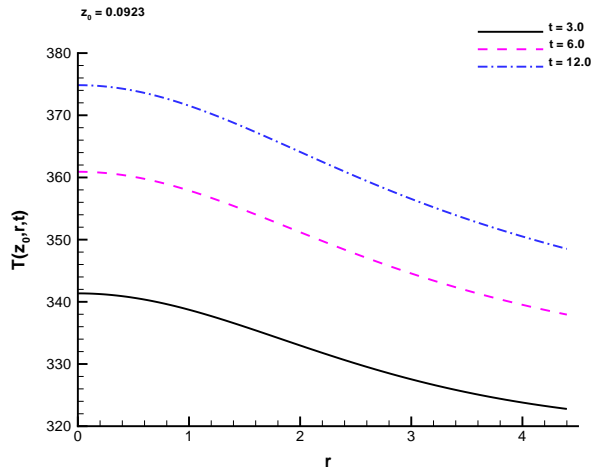
FIGURE 5.2. Temperature $\theta(z_0, r, t)$ as a function of the disc radius r ($[r] = cm$) for three different times, where z is fixed equal to $z_0 = 0.0923$ cm. The rim length is $r_{rim} = 0$ for this simulation.

(lower curve) boundary functions $h_1(t)$ and $h_2(t)$ – sometimes call center and edge temperature – are monitored with respect to time at the location $z_0 = 9.23 \cdot 10^{-2}$ cm. We note that the rim length $r_{rim} = R_0 - R_1$ for this simulation is set equal to zero. The temperature dependence $\theta(z_0, r, t)$ for this case as a function of the
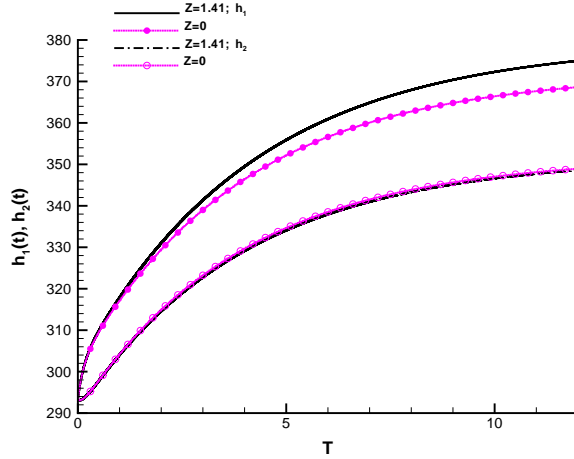

FIGURE 5.3. Bottom and top boundary functions $h_1(t)$ and $h_2(t)$ with respect to time (measured in seconds) for $Z_1 = Z_2 = 1.41$ (lines) and $Z_1 = Z_2 = 0$ (symbols). The rim length is $r_{rim} = 0$ for this simulation.

disc radius r is depicted in Figure 5.2 for the times $t = 3$ s (solid), $t = 6$ s (dashed) and $t = 12$ s (dashed-dotted curve). From these two figures it is obvious that the convergence towards the steady-state temperature is relatively slow.

The influence of the temperature dependence of the thermal conductivities to the temperature field is investigated in Figure 5.3. From this figure we recognise that the top temperatures $h_2(t)$ for $Z_i = 1.41$ and $Z_i = 0$ (cf., equation (5.12)) are nearly identical. However, the center temperature $h_1(t)$ obtained with $Z_i = 1.41$ is clearly above this one computed with constant thermal conductivities ($Z_i = 0$).

In Figure 5.4 a comparison between an implicit (solid and dashed lines) and an explicit (symbols) simulation for the center $h_1(t)$ and edge $h_2(t)$ temperature is shown. In order to compare both integration methods, we use now a coarser discretisation of the computational domain established by $J \times K = 6 \times 132$ nodes. Due to the CFL condition (see above), the time step size for the explicit computation is restricted to $\Delta t = 2.5 \cdot 10^{-5}$ s. For implicit methods there is, in principle, no such step size restriction. However, in general this may not be true and, hence, we fix the time step size equal to $2 \cdot 10^{-4}$ s, which is eight times larger than that one used for the explicit calculation. We monitor the numerical solution up to 5 s, which is equivalent to 200000 and 25000 temporal iteration cycles for the explicit and implicit computation, respectively. From the results seen in Figure 5.4, we finally conclude that the agreement between implicit and explicit simulation is very good. However, a very careful inspection reveals in the long-time limit, that the explicit results are slightly above those one computed in an implicit manner.
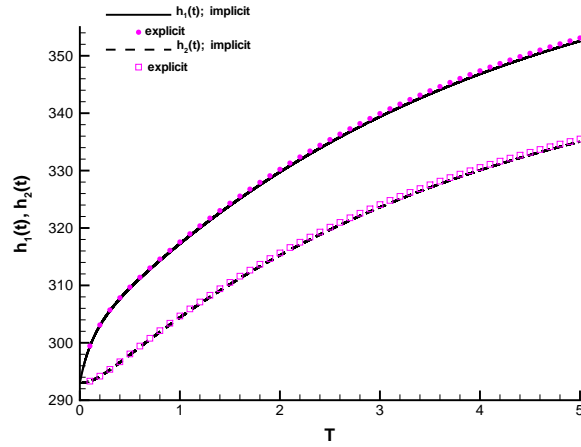
FIGURE 5.4. Comparison between an implicit (solid and dashed lines) and explicit (symbols) numerical simulation monitored at $z_0 = 0.1$ cm for the center $h_1(t)$ and edge $h_2(t)$ temperature. The time is measured in seconds and the time steps size for the implicit and explicit computation is $\Delta t = 2 \cdot 10^{-4}$ s and $\Delta t = 2.5 \cdot 10^{-5}$ s, respectively. The computational domain is discretised by a $J \times K = 6 \times 132$ mesh and the rim length is $r_{rim} = 0$.

EXPERIMENT 2 and 3:

These two experiments are performed in order to study the influence of the so-called cooling rim, which is placed at the left and right border of the computational domain in the range $R_1 \leq r \leq R_0$. This part of the diamond window is cooled down by water of temperature θ_{cool} in the same way as at the top of the disc. Besides
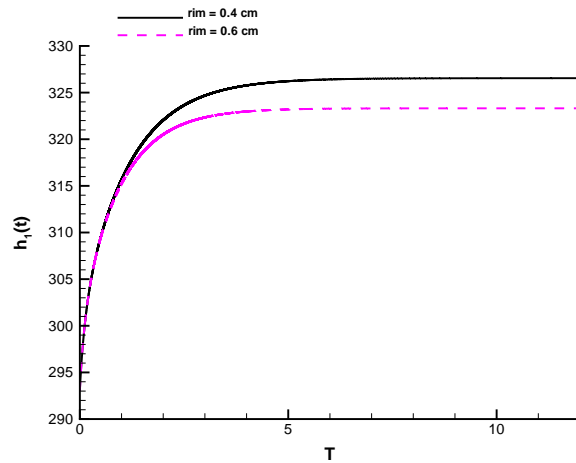

FIGURE 5.5. Central disc temperature $h_1(t) = \theta(z_0, 0, t)$ as a function of time (measured in seconds) for the rim length $r_{rim} = 0.4$ cm (solid) and $r_{rim} = 0.6$ cm (dashed curve).
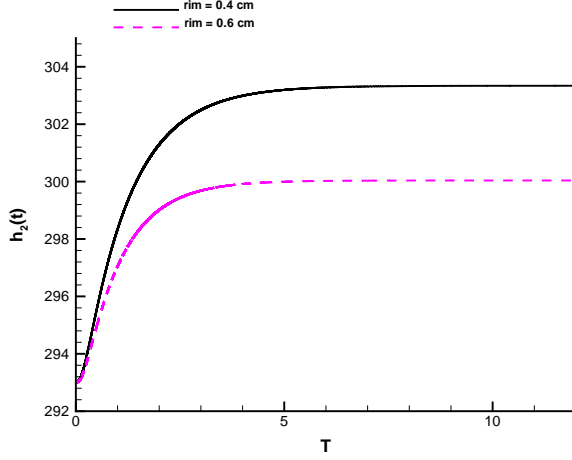
FIGURE 5.6. Edge disc temperature $h_2(t) = \theta(z_0, R_0, t)$ as a function of time (measured in seconds) for the rim length $r_{rim} = 0.4$ cm (solid) and $r_{rim} = 0.6$ cm (dashed curve).

the boundary condition already specified by the expression (5.18), we impose the mixed updating prescription of the border values given by

$$g_1(r_k, t) = \begin{cases} \theta_{1,k}(t) - \Delta z \frac{\alpha_m}{(\mathsf{s}_1)_{1,k}} \left[\theta_{1,k}(t) - \theta_{cool}\right], & \text{for } R_1 < r \leq R_0 \\ \theta_{1,k}(t), & \text{for } r \leq R_1 \end{cases} \qquad (5.19)$$

and

$$g_2(r_k, t) = \begin{cases} \theta_{J-1,k}(t) - \Delta z \frac{\alpha_m}{(\mathsf{s}_1)_{J-1,k}} \left[\theta_{J-1,k}(t) - \theta_{cool}\right], & \text{for } R_1 < r \leq R_0 \\ \theta_{J-1,k}(t), & \text{for } r \leq R_1 \end{cases} \qquad (5.20)$$

which holds for all k and $t \geq 0$ at the left and right disc border, respectively. The rim length during the 2nd and 3rd numerical experiment was respectively fixed equal to $r_{rim} = R_0 - R_1 = 0.4$ cm and $r_{rim} = 0.6$ cm. The numerical results for the temporal evolution of the central $h_1(t) = \theta(z_0, 0, t)$ and edge $h_2(t) = \theta(z_0, R_0, t)$ temperatures are shown in Figure 5.5 and 5.6, respectively. It is demonstrated by these plots, that the steady-state is reached within approximately 5 s and, furthermore, that the maximum temperature is reduced for the large-rim case compared to the experiment where $r_{rim} = 0.4$ cm. Both the edge and the center temperature are reduced by approximately three degrees. The effect of different length of the cooling rim is also presented in Figure 5.7. There, the temperature $\theta(z_0, r, t)$ as a function of the disc radius r is recorded for three different rim sizes, namely, $r_{rim} = 0$ (solid), $r_{rim} = 0.4$ cm (dashed) and $r_{rim} = 0.6$ cm (dashed-dotted lines) at the diagnostic point $z_0 = 0.0923$ cm and at the time $t = 3$ s. Figure 5.7 clearly indicates that the temperature profiles are drastically reduced if the cooling rim is included.

EXPERIMENT 4:

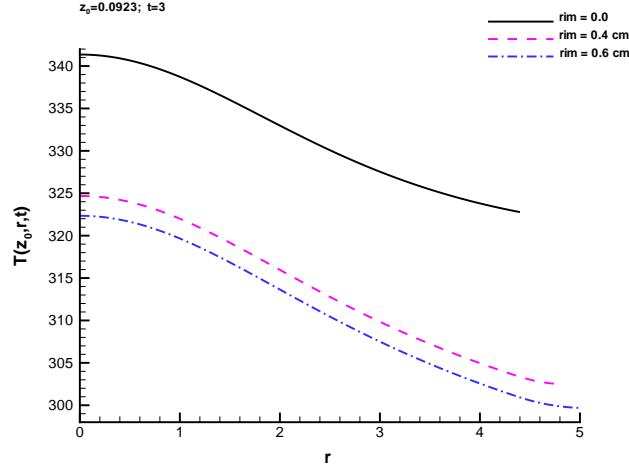For this simulation the occuring radii (cf. Figure 2.1) are fixed according to

FIGURE 5.7. Temperature $\theta(z_0, r, t)$ as a function of the disc radius r ($[r] = cm$) recorded at $z_0 = 0.0923$ cm and at $t = 3$ s for three different cooling rim lengths: Solid: $r_{rim} = 0$; dashed: $r_{rim} = 0.4$ cm; dashed-dotted: $r_{rim} = 0.6$ cm.

$R_A = 4.0$ cm, $R_1 = 4.4$ cm and $R_0 = 4.8$ cm. In addition to the cooling rim located at $R_1 \leq r \leq R_0$ we consider in this experiment an additional "radiation" area between R_A and R_1. At this surface we assume a power change due to conduction, which is described similarly to those given by the expression (5.7). The temperature of the cooling medium is $\theta_{cool} = 293$ K while the heat transfer coefficient is now chosen to be two times larger than α_m listed in Table 5.2: $\tilde{\alpha}_m = 2 \cdot \alpha$.

For the numerical calculation we pose the condition given by equation (5.18) at
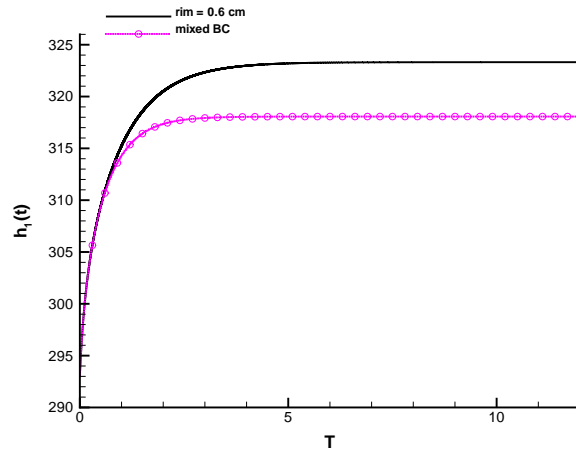

FIGURE 5.8. Center temperature $h_1(t)$ as a function of time (measured in seconds). Solid: $r_{rim} = 0.6$ cm; dashed-dotted: mixed boundary conditions on the left and right border of the domain.
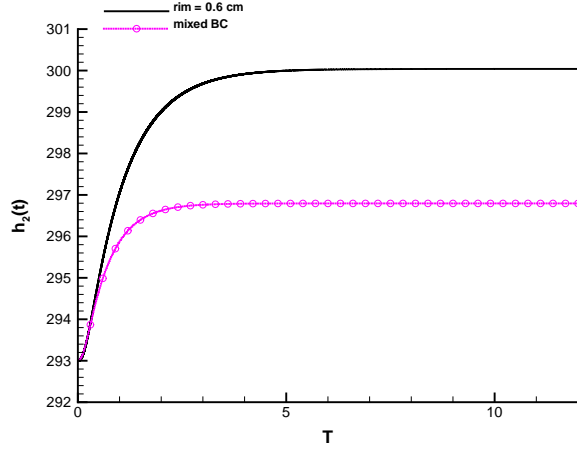
36

FIGURE 5.9. Edge temperature $h_2(t)$ as a function of time (measured in seconds). Solid: $r_{rim} = 0.6$ cm; dashed-dotted: mixed boundary conditions on the left and right border of the domain.

the top of the domain. At the left and right border of the computational domain the conditions

$$g_1(r_k, t) = \begin{cases} \theta_{1,k}(t) & \text{for } r \leq R_A \\ \theta_{1,k}(t) - \Delta z \frac{\bar{\alpha}_m}{(\mathsf{s}_1)_{1,k}} \left[\theta_{1,k}(t) - \theta_{cool} \right], & \text{for } R_A < r \leq R_1 \\ \theta_{1,k}(t) - \Delta z \frac{\alpha_m}{(\mathsf{s}_1)_{1,k}} \left[\theta_{1,k}(t) - \theta_{cool} \right], & \text{for } R_1 < r \leq R_0 \end{cases} \quad (5.21)$$

and

$$g_2(r_k, t) = \begin{cases} \theta_{J-1,k}(t), & \text{for } r \leq R_A \\ \theta_{J-1,k}(t) - \Delta z \frac{\bar{\alpha}_m}{(\mathsf{s}_1)_{J-1,k}} \left[\theta_{J-1,k}(t) - \theta_{cool} \right], & \text{for } R_A < r \leq R_1 \\ \theta_{J-1,k}(t) - \Delta z \frac{\alpha_m}{(\mathsf{s}_1)_{J-1,k}} \left[\theta_{J-1,k}(t) - \theta_{cool} \right], & \text{for } R_1 < r \leq R_0 \end{cases}$$
$$(5.22)$$

for all k and $t \geq 0$ are established, which are called "mixed boundary" conditions. The effect of these conditions on the center and edge temperature is seen in Figures 5.8 and 5.9. There, we observe that the steady-state bottom $h_1(t)$ and top $h_2(t)$ temperature for the mixed boundary case drops of five and three degrees, respectively, below those obtained from computations where the rim size is $r_{rim} = 0.6$ cm.

EXPERIMENT 5:

The intention of this simulation experiment is to demonstrate the possibility to consider real two-dimensional effects. This means, that we are now interested in the simulation of a thick ($D = 0.8$ cm) model window, for which the reference conductivities are reduced by a factor of six ($\mathsf{s}_{1,R} = \mathsf{s}_{2,R} = 3 \frac{W}{cm\,K}$) while the radii are the same as in the previous experiment. To establish an asymmetry, we use mixed boundary conditions at the left border of the computational domain as given by the updating prescription (5.21). At the right boundary of the domain we impose
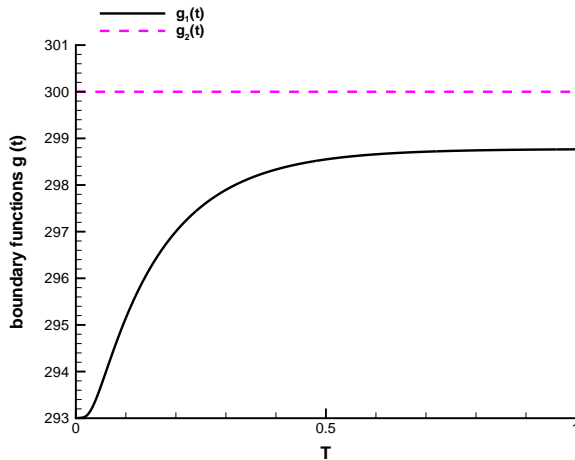
FIGURE 5.10. Left (solid) and right (dashed line) boundary temperature $g_1(t) = \theta(0, r_0, t)$ and $g_2(t) = \theta(D, r_0, t)$, respectively, with restect to time (measured in seconds). The results are recorded at the diagnostic points $(z, r_0) = (0, 4)$ and $(z, r_0) = (0.8, 4)$. Mixed boundary conditions are specified on the left border of the domain while the temperatre is constant equal to $g_2(t) = 300$ K.

a constant temperature condition according to

$$g_2(r_k, t) = 300 \text{ K} \tag{5.23}$$

for all k and $t \geq 0$. In Figure 5.10, these boundary temperatures are monitored with respect to time at the diagnostic points $(z, r_0) = (0, 4.0)$ cm and $(z, r_0) = (0.8, 4.0)$ cm. It is obvious from this plot, that the steady-state temperature between the left (solid) and right (dashed line) border differ by about two degrees. This difference is now responsible for a temperature distribution, which depends also on the z-coordinate. The spatial temperature dependence for the thick model window obtained from the simulation is depicted in Figure 5.11. Additionally from these two contour snapshots recorded at $t = 0.25$ s (left) and $t = 1.0$ s (right plot), we get an impression of the temporal evolution of the spatial temperatur distribution.

For the implicit computations of the yet presented simulation, the time step size was fixed equal to $\Delta t = 2 \cdot 10^{-4}$ s and the domain was discretised by $J \times K = 53 \times 316$ computation nodes.

6. CONCLUDING REMARKS

In the present paper we describe a computer program development for the numerical solution of the two-dimensional transient diffusion equation for rotationally symmetric domains in the (z, r)-plane. In this context the spatial derivatives of the mathematical model are approximated by applying standard finite-difference methods. The temporal treatment of the diffusion is modelled by explicit and implicit integration techniques. The implemented algorithms make use of Cartesian
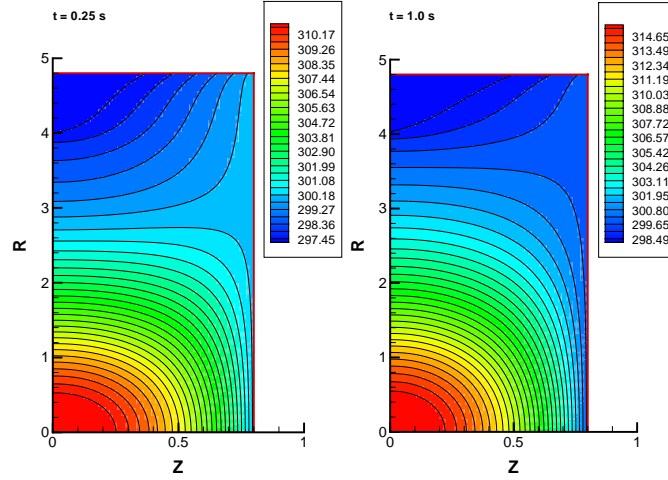
FIGURE 5.11. Spatial temperature distribution in a thick model window recorded at $t = 0.25$ s (left) and $t = 1.0$ s (right plot). During the simulation experiment mixed boundary values are established at the left border while constant data (300 K) are prescribed at the right side. Discretisation: $J \times K = 53 \times 316$; time-step size: $\Delta t = 2 \cdot 10^{-4}$ s.

grid arrangements, which are, in general, less flexible to map realistic geometries to a discrete image, but which are sufficient for the applications considered here. However, for further applications of the diffusion equation solver it seemed to be desirable to perform computations for more complex geometries. In particular, this aspect may be important when the millimeterwave radiation, for instance, does not meet the center of the diamond disc window. Obviously this means, that the power distribution in the material can no longer be modelled by an azimuthally symmetric (Gaussian) profile.

An attractive approach to solve the two-dimensional diffusion equation in irregular geometries with the Cartesian finite-volume method was recently proposed by Calhoun and LeVeque [2]. This very effective method avoids difficulties connected with unstructured mesh generation by using a Cartesian grid where the physical domain – in general, a complex geometry – is embedded. Detailed considerations have to be carried out to adapt such a fully conservative, finite-volume scheme for the diffusion problem in complex computational domains.

ACKNOWLEGEMENTS

REFERENCES

[1] D. Anderson, J. Tannehill, and P. R.H., *Computational Fluid Mechanics and Heat Transfer*, McGraw-Hill, New York, 1984.

[2] D. Calhoun and R. LeVeque, *A Cartesian grid finite-volume method for the advection-diffusion equation in irregular geometries*, J. Comput. Phys., 157 (2000), pp. 143–180.

[3] R. Courant, K. Friedrichs, and H. Lewy, *Über die partiellen Differentialgleichungen der mathematischen Physik*, Math. Annalen, 100 (1928), pp. 31–74.

[4] J. Crank and P. Nicholson, *A practical method for numerical evaluation of solutions of partial differential equations of the heat condution*, Proc. Camb. Phil. Soc., 43 (1947), pp. 50–67.

[5] J. Faires and R. Burdon, *Numerische Methoden*, Spektrum Akademischer Verlag, Heidelberg, 1994.

[6] L. Feher, *Simulationsrechnungen zur verfahrenstechnischen Anwendungen von Millimeterwellen für die industrielle Materialprozesstechnik*, Forschungszentrum Karlsruhe – Technik und Umwelt, **FZKA 5885**, (1997).

[7] S. Gottlieb and C.-W. Shu, *Total variation diminishing Runge-Kutta schemes*, Mathematics of Computation, 67 (1998), pp. 73–85.

[8] E. Hairer, S. Norsett, and G. Wanner, *Solving Ordinary Differential Equations I*, Springer, Berlin, 1993.

[9] H.-U. Nickel, *Hochfrequenztechnische Aspekte zur Entwicklung rückwirkungsarmer Ausgangsfenster für Millimeterwellen-Gyrotrons hoher Leistung*, Forschungszentrum Karlsruhe – Technik und Umwelt, **FZKA 5513**, (1995).

[10] M. Özisik, *Heat Conduction*, Wiley, New York, 1993.

[11] W. H. Press, B. P. Flannery, S. A. Teukolsky, and W. T. Vetterling, *Numerical Recipes*, Cambridge University Press, Cambridge, 1987.

[12] E. Saatdjian, *Transport Phenomena*, Wiley, Chichester, 2000.

[13] R. Schneider, *Finite-volume approach for the diffusion equation on Cartesian grids for complex geometries*, in preparation, (2003).

[14] C.-W. Shu and S. Osher, *Efficient implementation of essentially non-oscillatory shock capturing schemes I*, J. Comput. Phys., 77 (1988), pp. 439–471.

[15] ———, *Efficient implementation of essentially non-oscillatory shock capturing schemes II*, J. Comput. Phys., 83 (1989), pp. 32–78.

[16] V. Singh, A. Arnold, E. Borie, O. Braz, and M. Thumm, *Thermal modelling of edge-cooled single disc gyrotron windows using a one-dimensional finite difference computer code*, Int. J. Infrared and Millimeter Waves, 19 (1998), pp. 1451–1469.

[17] G. Smith, *Numerical Solution of Partial Differential Equations: Finite Difference Methods*, Oxford Applied Mathematics and Computing Science Series; Clarendon Press, Oxford, 1990.

[18] R. Spiegel, *Wärmeübertragung durch Strahlung*, Springer, Vol.1 and Vol.2, Heidelberg, 1988.

[19] M. Thumm, *MPACVD-diamond windows for high-power and long-pulse millimeter wave transmission*, Diamond and Related Materials, 10 (2001), pp. 1692–1699.